High-Q UHF Spoke-Supported Ring Resonators

Thura Lin Naing, *Member, IEEE*, Tristan O. Rocheleau, *Member, IEEE*, Zeying Ren, *Member, IEEE*, Sheng-Shian Li, *Member, IEEE*, and Clark T.-C. Nguyen, *Fellow, IEEE*

***Abstract*— A vibrating micromechanical spoke-supported ring resonator employing a central peg-anchor, balanced non-intrusive quarter-wavelength extensional support beams, and notched support attachments attains high Q-factor in vacuum, posting 10 000 at 441 MHz when made of polysilicon structural material and 42 900 at 2.97 GHz when made of microcrystalline diamond. The latter marks the highest $f \cdot Q$ of 1.27×10^{14} for any acoustic resonator at room temperature, besting even macroscopic bulk-mode devices. Very high Q values like these in a device occupying only 870 μm^2 pave a path toward on-chip realizations of RF channelizers and ultra-low phase-noise gigahertz oscillators for secure communications. With frequency determined by lithographically defined ring-width rather than radius, a capacitive transducer with a 75-nm gap allows this 2.97-GHz version to achieve a series motional resistance of 81 kΩ. Though still higher than desired, this marks a 30× improvement over previous pure polysilicon surface-micromachined solid disk resonators in the gigahertz range, and if predicted performance-scaling holds true, seven such resonators constructed in a mechanically coupled array with 30-nm gap spacing, could lower this to only 300 Ω. Confidence in a prediction like this stems from the confirmed accuracy of the electrical equivalent circuit described herein that models not only the ring and its transducers, but also its supports. [2015-0132]**

***Index Terms*— Microelectromechanical systems (MEMS), ultra-high frequency (UHF), micromechanical resonator, quarter-wavelength, high-Q, diamond, polysilicon, bandpass filter.**

I. Introduction

HIGH-Q resonators operating at GHz frequencies could greatly simplify wireless communication receivers if filters constructed of these resonators could select communication channels (rather than bands of channels) right at RF, immediately after the antenna, with out-of-channel noise and interferers removed before the received signal reaches any transistor circuits [1], [2]. With such an RF channel-selection capability, a wireless receiver might dispense with multi-stage down-conversion circuits, and instead, utilize a direct sampling A/D converter at the front end, allowing signals to be processed digitally much earlier in the receive path, thereby making possible a true software-defined radio [3], [4] without the need for power-hungry, wideband digitization. In more conventional analog front-ends, RF channel-selection stands to relax dynamic range requirements towards substantially lower power communications, especially for low data rate applications, like autonomous sensor networks.

Unfortunately, RF channel-selection constitutes an extremely challenging prospect, since it generally requires bandwidth selectivity on the order of 0.1% or less, which in turn requires filters using resonators with Q's >10,000 to maintain acceptable insertion loss (below 2 dB) [5], [6]. For example, a three-resonator 1-MHz bandwidth Chebyshev filter centered at 3-GHz corresponds to a 0.03%-bandwidth for which achieving 2-dB insertion loss calls for constituent resonator Q's >30,000 [4], [6], [7]. On the bright side, the small percent bandwidth calls for an electromechanical coupling efficiency of only 0.075% to avoid undue passband distortion from shunt capacitance. This means channel-selection puts a much higher premium on Q than electromechanical coupling. Beyond sheer Q and a modest amount of coupling, channel-selection requires either a tunable front-end filter or a bank of many (e.g., hundreds) of switchable filters that cover the needed frequency range.

Off-chip high-Q resonators in use today, such as surface acoustic wave (SAW) filters or thin-film bulk acoustic resonator (FBAR) filters, fall well short of these requirements. In particular, while their electromechanical couplings of 5-7% are well in excess of what's needed, their Q's are generally an order of magnitude lower than required. Here, the fact that FBAR's post very high figure of merits like k_{eff}^2-Q, yet still do not satisfy channel-select requirements, attests to the limited utility or even misdirection of such metrics. Indeed, k_{eff}^2-Q is really not an effective metric to evaluate a given resonator for use in filter design; rather, knowledge of the specific values of k_{eff}^2 and Q is needed. Aside from Q, SAW or FBAR frequencies are not sufficiently tunable for a tuned front-end filter approach. On the other hand, FBAR's are small enough to implement a multiple-filter bank. However, they are not amenable to integration of all filters onto a single chip, since their frequencies are governed primarily by film thickness. This means a different film deposition, shadow-masking, or etch-back step is required for each filter center frequency in the bank—clearly, an expensive prospect if hundreds of RF channel-select filters are required.

On the other hand, several recently demonstrated MEMS-based high-Q vibrating resonators [8]–[14], while

Manuscript received May 14, 2015; revised August 20, 2015; accepted August 27, 2015. Date of publication November 11, 2015; date of current version February 1, 2016. This work was supported in part by the Defense Advanced Research Projects Agency, in part by the Engineering Research Center on Wireless Integrated Microsystems through the National Science Foundation, and in part by the U.S. Department of Defense. Subject Editor L. Buchaillot. *(Corresponding author: Thura Lin Naing.)*

T. L. Naing, T. O. Rocheleau, and C. T.-C. Nguyen are with the Department of Electrical Engineering and Computer Sciences, University of California at Berkeley, Berkeley, CA 94720 USA (e-mail: mchiplin@gmail.com; tristan.rocheleau@gmail.com; ctnguyen@eecs.berkeley.edu).

Z. Ren was formerly with the University of Michigan, Ann Arbor, MI 48109 USA. She is now with Crossbar, Inc., Santa Clara, CA 95054 USA.

S.-S. Li was formerly with the University of Michigan, Ann Arbor, MI 48109 USA. He is now with the Institute of NanoEngineering and MicroSystems, National Tsing Hua University, Hsinchu 30013, Taiwan (e-mail: ssli@mx.nthu.edu.tw).

Color versions of one or more of the figures in this paper are available online at http://ieeexplore.ieee.org.

Digital Object Identifier 10.1109/JMEMS.2015.2480395

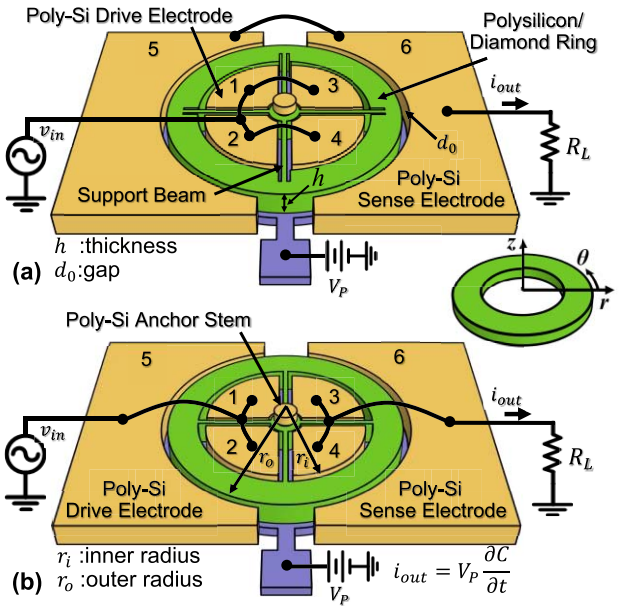

Fig. 1. Perspective views of ring resonators in typical two-port bias schemes for (a) electrode configuration A; and (b) electrode configuration B.

still not sufficiently tunable for a tuned filter approach, exhibit resonance frequencies governed by lateral dimensions, which means hundreds or more different frequencies can be realized in one film layer on a single planar-processed chip by mere specification of their lateral dimensions via computer-aided-design (CAD) layout. Of these resonators, only the capacitive-gap transduced CVD diamond disks of [14] attain without overmoding Q's greater than 10,000 at frequencies exceeding 1 GHz, in both air and vacuum, but at the cost of motional resistance exceeding 100 kΩ. A recent filter using similar capacitive-gap transduced disk resonators that already demonstrates sufficient Q and coupling to realize 0.1% bandwidth filters with high stop-band rejection at 223 MHz [7] with only 590 Ω of required termination resistance provides encouragement to efforts towards similar performance at frequencies past 1 GHz. In the meantime, even higher Q's than the 12,000 demonstrated in [14] are needed.

Pursuant to achieving high Q values at GHz frequencies with lower motional resistance, Li *et al.* [15] introduced the first radial ring resonator that utilized a centralized spoke-supported structure to greatly reduce support loss towards pure polysilicon ring resonator Q's in excess of 10,000 at frequencies past 1 GHz. The specific design, shown in Fig. 1(a), was previously dubbed the "hollow-disk" ring resonator in [15], since it was conceived of by removing quadrants of material from a solid disk resonator, but purposely leaving intact beams of material to non-intrusively support the ring structure. Similar devices when constructed in diamond [16] have now pushed performance even further, with Q's above 40,000 at frequencies approaching 3 GHz. Specifically, the design of Fig. 1(b) constructed in microcrystalline diamond achieves a Q of 42,900 at 2.97 GHz, which is now high enough to make possible RF channel-select filters with less than 1 dB of insertion loss. With electrodes both inside and outside the spoke-supported ring structure, this design attains electrode overlap advantages similar to that of a previously published annular ring [17] and extensional wine-glass mode ring designs [13], while offering a much less intrusive support structure that not only enables substantially higher Q, but also enables measured impedances as low as 81 kΩ with 75-nm electrode-to-resonator gaps. This marks a 30× reduction in impedance from previous surface-micromachined, pure polysilicon, solid-disk resonators operating past 1 GHz [12], with similar gap spacing.

Aside from providing a complete set of measured data for spoke-supported rings constructed in both polysilicon and polydiamond in Section VI, this paper presents the complete design flow needed to realize a given frequency and impedance performance in Sections II-IV, as well as an equivalent circuit in Section V that models not only the resonance vibration and electromechanical coupling characteristics of the device, but also the influence of its support and anchors. In particular, comparison between theory, simulation, and measurement in Section IV and VI gauges the importance of quarter-wavelength support design in setting the maximum Q while inducing the smallest shift in resonance frequency from the ideal "levitated" condition. Section VI finally uses the confirmed model to project what might be possible with this device with regards to the ultimate frequency, Q, and electromechanical coupling available for practical applications.

II. Device Structure and Operation

Fig. 1(a) presents the perspective-view schematic of a spoke-supported ring under a two-port bias, excitation, and measurement scheme, identifying key features to be used later for analysis. As shown, this device consists of a ring structure constructed in doped polysilicon or diamond, with thickness h, inner radius r_i, and outer radius r_o, suspended by spokes emanating from an anchored stem self-aligned to the very center of the structure [12]. Here, the use of a centrally-located anchor with radially emanating longitudinal-mode, quarter-wavelength support beams provides a degree of balance and isolation that greatly suppresses anchor losses to the substrate, allowing this annular ring-type resonator to achieve Q's much higher than versions where the ring vibrating in radial-contour modes is directly anchored to the substrate from underneath [17]; or where the ring vibrating in extensional wine-glass modes is supported by tethers (i.e., support beams) at its quasi-nodal points [13]. As will be detailed later, the support beams are designed with geometries that isolate the resonator structure from its anchors in order to minimize energy losses to the substrate, allowing the structure to maintain exceptionally high Q.

A. Excitation and Detection

The spoke-supported ring is surrounded by inner and outer doped polysilicon capacitive transducer electrodes spaced less than 100 nm from its inner and outer edges, respectively. To excite the device of Fig. 1(a) in its two-port configuration, a dc-bias voltage V_P is applied to the conductive ring and an

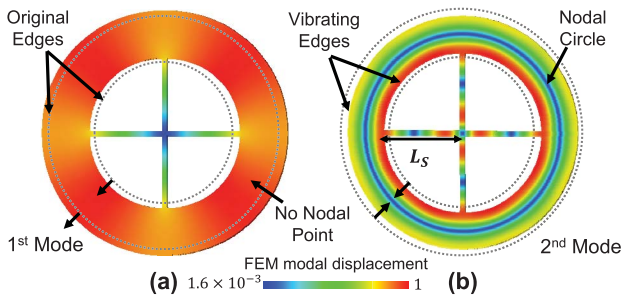

Fig. 2. Finite element simulated modes for the spoke-supported ring resonator and extensional support beam of Fig. 1(b). (a) 1st contour mode (symmetric). (b) 2nd contour mode (anti-symmetric).

ac signal v_{in} to its inner (i.e., drive or input) electrodes. Note that the application of the dc-bias V_P serves only to charge the electrode-to-resonator capacitance. No dc current flows, so no dc power is consumed. Together, these voltages applied across the small inner capacitive gaps generate a radial electrostatic input force F_{in} at the frequency of v_{in} given by

$$F_{in} = \frac{1}{2}\left(\frac{\partial C_{o,in}}{\partial r}\right)(V_P - v_{in})^2 \cong -V_P\left(\frac{\partial C_{o,in}}{\partial r}\right)v_{in} \quad (1)$$

where the rightmost form retains only the ac term at the frequency of v_{in}. $\partial C_{o,in}/\partial r$ is the change in electrode-to-resonator overlap capacitance per unit radial displacement at the input port, given under a small-signal parallel-plate approximation as

$$\frac{\partial C_{o,in}}{\partial r} = \frac{\varepsilon_0 A_{in}}{d_o^2} \quad (2)$$

where A_{in} is the combined static electrode-to-resonator overlap area of all input ports in the hookup of Fig. 1(a), and d_o is the electrode-to-resonator gap spacing. When the frequency of v_{in} matches that of one of the resonance modes, the resulting force applied to the inner perimeter drives the ring into the vibration mode shape of that mode. Fig. 2 presents the first two radial-contour mode shapes, the second of which is of most interest here, since it offers a balanced shape with a nodal circle that helps to maximize Q. As shown, this mode shape expands and contracts radially around a nodal circle within the ring, with the ring's inner and outer perimeters moving in phase and in opposite directions, with a zero-to-peak resonance radial displacement amplitude at the inner perimeter given by

$$\Re\,(r_i) = \frac{QF_{in}}{k_{rei}} = \frac{Q}{k_{rei}}V_P\frac{\partial C_{o,in}}{\partial r}v_{in} \quad (3)$$

where k_{rei} is the equivalent dynamic stiffness at a location along the inner perimeter of the ring (for force on the inner edge of the ring as in Fig. 1(a)—a force on the outer perimeter would require stiffness evaluated on the outer edge) that includes both mechanical and electrical [18] components. Assuming a radial-contour mode shape, e.g., no θ dependence, the corresponding resonance displacement amplitude at the outer perimeter is then given by

$$\Re\,(r_o) = \frac{\Re_{mode}\,(r_o)}{\Re_{mode}\,(r_i)}\Re\,(r_i) = \frac{\Re_{mode}\,(r_o)}{\Re_{mode}\,(r_i)}\frac{QV_P}{k_{rei}}\frac{\partial C_{o,in}}{\partial r}v_{in} \quad (4)$$

where $\Re_{mode}(r)$ is a function describing the relative radial displacement in the mode shape of the ring at radial location r, given later in Section III.

The radial vibration of the spoke-supported ring at the outer perimeter in turn creates a dc-biased (by V_P) time-varying capacitance between the outer edge of the ring and its output (i.e., sense) electrode. This varying capacitance then sources an output current i_{out} proportional to the amplitude of vibration at the outer perimeter of the ring, with resonance magnitude given in phasor form by

$$\begin{aligned} i_{out} &= V_P\frac{\partial C_{o,out}}{\partial r}\frac{\partial \Re\,(r_o)}{\partial t} \\ &= \frac{\Re_{mode}\,(r_o)}{\Re_{mode}\,(r_i)}\frac{Q\omega_o}{k_{rei}}\frac{\partial C_{o,in}}{\partial r}\frac{\partial C_{o,out}}{\partial r}V_P^2 v_{in} \end{aligned} \quad (5)$$

where (4) has been used; $\partial C_{o,out}/\partial r$ is the change in electrode-to-resonator overlap capacitance per unit radial displacement at the output port; and where the output electrode is assumed grounded. The output current is proportional to the change in electrode-to-resonator overlap capacitance per unit radial displacement at both the input and output ports, and inversely proportional to the equivalent dynamic stiffness.

As derived, (5) corresponds to the case where the input force is applied at precisely the resonance frequency of the spoke-supported ring. This can be further simplified through the introduction of the equivalent series motional resistance of the device, R_x, given by

$$R_x = \frac{v_{in}}{i_{out}} = \frac{k_{rei}}{Q\omega_o\frac{\partial C_{o,in}}{\partial r}\frac{\partial C_{o,out}}{\partial r}V_P^2}\frac{\Re_{mode}\,(r_i)}{\Re_{mode}\,(r_o)} \quad (6)$$

With this substitution and incorporating the standard Lorentzian frequency response of any resonator, the overall transfer function from input voltage to output current becomes the well-known bandpass biquad

$$\frac{i_{out}}{v_{in}} = \frac{1}{R_x}\frac{(\omega_o/Q)\,s}{s^2 + (\omega_o/Q)\,s + \omega_o^2} \quad (7)$$

The electrical response of the resonator in the hook-up of Fig. 1(a) thus equates to that of a single *LCR* electrical circuit. In short, via action of the spoke-supported ring resonator, the electrical input signal v_{in} is converted to a mechanical signal at the input port, filtered (with high Q) in the mechanical domain, then re-converted to an electrical signal at the output port, ready for further processing by subsequent stages.

B. On-Off Switchability

As with other capacitively transduced resonators, note that output current ensues only if the dc-bias voltage V_P is non-zero. If the dc-bias voltage between the output electrode and the ring is zero, then no current flows, and the device is effectively "off." Thus, V_P provides an on/off "self-switching" for this device that removes the need for external switches in multi-band RF front-end architectures [19].

III. Resonator Frequency Design

Having described the qualitative operational aspects of the spoke-supported ring, analytical formulations governing the precise frequency design of this device are now in order. Following the approach of [20], this analysis assumes that the ring thickness is thin compared to its lateral dimensions ($h \ll r_i$). The analysis further assumes that the top and bottom faces of the ring are free of intrinsic stress; and since the structure is thin and forces are applied in only the lateral directions, the vertical stress components also vanish throughout its bulk.

With these assumptions, and given axial-symmetry, i.e., $\partial u_r/\partial\theta = 0$, and $u_\theta = 0$, the constitutive equations for the stress tensor T_{ij} of an ideal ring, such as depicted in inset of Fig. 1(a), reduce to [20]

$$\begin{aligned} T_{rr} &= c_{11}^E \frac{\partial u_r}{\partial r} + c_{12}^E \frac{u_r}{r} \\ T_{\theta\theta} &= c_{12}^E \frac{\partial u_r}{\partial r} + c_{11}^E \frac{u_r}{r}; \quad T_{r\theta} = 0 \end{aligned} \tag{8}$$

where u_r is the displacement along the radial direction. c_{11}^E and c_{12}^E are elastic stiffness constants to be defined in detail later. Substituting the stress components of (8) into the radial form of the wave equation given by [20] yields

$$c_{11}^E \left[\frac{\partial^2 u_r}{\partial r^2} + \frac{1}{r}\frac{\partial u_r}{\partial r} - \frac{u_r}{r^2} \right] = \rho \ddot{u}_r \tag{9}$$

where ρ is the mass density of the ring structural material. Assuming that the ring is driven by an ac voltage $v_{in} = V_{in} e^{j\omega t}$, it follows that

$$\frac{\partial^2 U_r}{\partial r^2} + \frac{1}{r}\frac{\partial U_r}{\partial r} + \left[\frac{\omega^2}{(v^p)^2} - \frac{1}{r^2} \right] U_r = 0 \tag{10}$$

where $v^p = \sqrt{c_{11}^E/\rho}$ is the acoustic velocity of the material, and where c_{11}^E can now be interpreted as its Young's modulus. The general solution of (10) for contour modes becomes

$$U_r = \Re(r) \cdot e^{j\omega t} = [M J_1(pr) + N Y_1(pr)]\, e^{j\omega t} \tag{11}$$

which describes the mode shape of the ring at its different resonance frequencies assuming the effect of the support beams on ring motion is negligible, as can be achieved using the quarter-wavelength strategy discussed in Section IV. Here, $p = \omega_o/v^p$ is a frequency parameter, and J_n and Y_n represent nth order Bessel functions of the first and second kind, respectively. The constants M and N are chosen to satisfy the stress-free boundary conditions at the inner and outer edges of the ring

$$T_{rr} = 0 \qquad \text{at } r = r_i \text{ and } r = r_o \tag{12}$$

Combining (8), (11), and (12), the ratio of constants N over M can be written

$$\begin{aligned} \frac{N}{M} &= -\frac{r_i G_J(r_o) - r_o G_J(r_i)}{r_i G_Y(r_o) - r_o G_Y(r_i)} \\ G_J(r) &= pr J_0(pr) - J_1(pr)(1-\sigma) \\ G_Y(r) &= pr Y_0(pr) - Y_1(pr)(1-\sigma) \end{aligned} \tag{13}$$

where $\sigma = c_{12}^E/c_{11}^E$ equates to a planar Poisson ratio. This is especially the case for the devices of this work, since their structural materials are isotropic in the plane normal to the z axis.

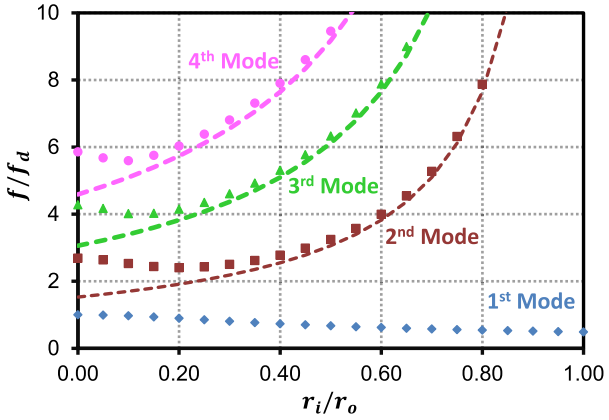

Fig. 3. Plot of the resonance frequency of a spoke-supported ring with $r_o = 20\ \mu$m and variable r_i in its 1st, 2nd, 3rd, and 4th modes. The dotted lines show the behavior using (16). f_d is the fundamental resonance frequency of a solid disk with radius r_o.

Use of (11) and (12) now yields the frequency equation

$$\begin{aligned} &[J_1(pr_i)\sigma - J_1(pr_i) + r_i p J_0(pr_i)] \\ &\quad \times [Y_1(pr_o)\sigma - Y_1(pr_o) + r_o p Y_0(pr_o)] \\ &\quad - [Y_1(pr_i)\sigma - Y_1(pr_i) + r_i p Y_0(pr_i)] \\ &\quad \times [J_1(pr_o)\sigma - J_1(pr_o) + r_o p J_0(pr_o)] = 0 \end{aligned} \tag{14}$$

After solving (14) to obtain frequency parameter p, the mechanical resonance frequency of the ring structure, f_{nom}, readily follows via

$$f_{nom} = \frac{\omega_{nom}}{2\pi} = \frac{p}{2\pi}\sqrt{\frac{E}{\rho\left(1-\sigma^2\right)}} \tag{15}$$

where ω_{nom} is the nominal radian mechanical resonance frequency, and E is the Young's modulus of the structural material. The first solution of (14) gives the first mode resonance of Fig. 2(a), and the second solution gives the second mode resonance of Fig. 2(b), and so forth.

Using (15), Fig. 3 plots (using dotted curves) the in-plane extensional resonance frequencies for a 2μm-thick ring with 20μm outer radius normalized to the fundamental mode frequency of a 20-μm-radius solid disk as a function of the ratio of inner radius-to-outer radius r_i/r_o and as a function of mode. Fig. 4 further presents several simulated curves describing the shapes associated with these modes. As expected, the resonance frequency of the first mode equals that of a thin disk [12] when $r_i/r_o = 0$, then decreases as r_i/r_o rises to a lowest point of 0.4867 times that of a disk when $r_i/r_o = 1$. Here, the first mode frequency approximately varies as the reciprocal of the average of the inner and outer radii of the structure and can be thought of as extensional around the contour of a "hollowed out" disk.

The higher radial-contour modes differ in that they are extensional around the width of the annulus, rather than the contour of the hollow disk. Their frequencies thus vary as the reciprocal of the annulus width ($r_o - r_i$), rather than average radius as for a disk resonator, effectively decoupling design

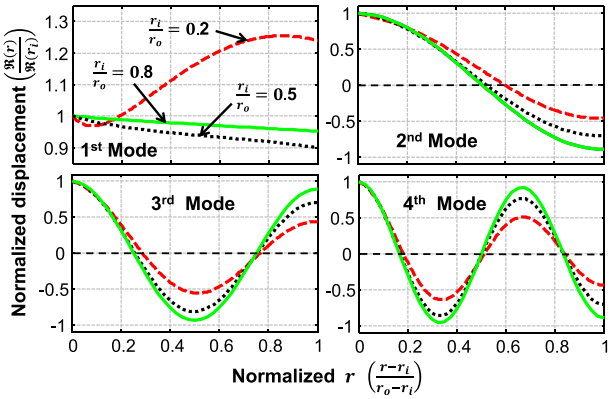

Fig. 4. The first, second, third, and forth mode shapes for spoke-supported rings with $r_i/r_o = 0.2$, $r_i/r_o = 0.5$, and $r_i/r_o = 0.8$, all with $r_o = 20$ μm.

criteria for frequency and impedance. Specifically, frequency depends mainly on ring width, and not average radius, while impedance depends mainly on average radius. This decoupling of frequency and impedance design opens the door for a capacitively-transduced resonator that simultaneously achieves GHz frequency and low impedance.

To capture the strong dependence of higher mode frequency on ring width, rather than average radius, (15) can be approximated by an expression for the higher extensional modes

$$f_{nom/approx.} = \frac{n-1}{2W_r}\sqrt{\frac{E}{\rho}}, \quad n = 2, 3, 4, \ldots \text{ for } \frac{r_i}{r_o} > \frac{1}{n} \tag{16}$$

where $W_r = (r_o - r_i)$ is the radial ring width, and n is the order of the vibration mode. The dashed curves in Fig. 3 are those generated by (16), which are seen to be accurate for $r_i/r_o > 1/n$. This expression is similar to the approximate expression for the extensional wine-glass ring (i.e., [13, eq. (6)]), except that the spoke-supported ring allows mode shapes for any integer value of n, rather than the solely odd values permitted by the extensional wine-glass ring solutions.

IV. Support Design

To maximize the ring's Q, loss must be minimized. Among loss mechanisms that influence Q, material and anchor loss are often among the most important at GHz frequencies. Though accurate predictive models are challenging, material loss typically manifests at these frequencies as phonon-phonon interactions [21], [22]. For this case, the high acoustic velocity and thermal conductivity of diamond gives it a marked advantage over other materials, with a predicted ceiling on Q of ~380,000 at 3 GHz [23], sufficiently high that one might expect material loss to be negligible, here.

If not properly designed, however, the support beams can still degrade the Q of the ring resonator through anchor loss, as well as perturb mode shape and resonance frequency. The key to maximizing practically all aspects of a resonator's performance is to minimize the influence of its support beams. Ultimately, the design that optimizes Q in fact also sets the resonance frequency equal to the value expected for an ideal ring with no supports and sets the mode shape to that expected for an unsupported (i.e., levitated) ring. The spoke support used in this work attempts to achieve "virtual levitation" [24] to provide a degree of anchor isolation far superior to its predecessors.

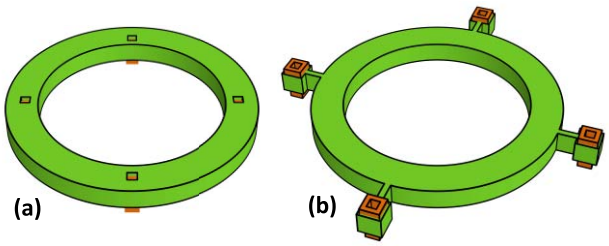

Fig. 5. Perspective-views of past resonator designs with (a) the radial ring resonator in [17] and (b) the extensional wine-glass ring resonator of [13].

A. Maximizing Resonator Q

To highlight the advantages of the spoke support used in this work, Fig. 5 presents two previous ring resonator support designs for comparison with the present design of Fig. 1. The first of these, in Fig. 5(a) locates anchors on the nodal line (actually, circle) of the second contour mode, i.e., of the mode in Fig. 2(b). Although locating anchors at nodal points—as done in [12] and some versions of [13] and [25]—does reduce energy transfer from a vibrating resonator to its anchors by virtue of the very little (ideally no) motion occurring at the nodes, some energy is still lost since the anchors are inevitably finite in size, and thus, still attach to non-nodal (i.e., moving) locations immediately around the nodal points.

The suspension design of Fig. 5(b) solves this problem by taking advantage of the transmission line-like behavior of its support beams at high frequency and dimensions them to correspond to effective quarter-wavelengths that then generate acoustic impedance-mismatches between the ring resonator and its anchors, reflecting wave energy back into the ring structure, minimizing energy losses, and maximizing the system Q.

The use of quarter-wavelength supports to maximize the Q's of micromechanical resonators and filters is well documented in the literature [13], [24], [26]. Indeed, the basic strategy of dimensioning a support to correspond to an odd multiple of a quarter wavelength at the frequency of resonance in order to transform the (ideally) infinite mechanical impedance at a fixed anchor to zero impedance at the support-to-resonator attachment location, has been instrumental here in attaining the highest Q micromechanical resonators, to date. In effect, if the supports can be made to present zero acoustic impedances at locations where they attach to a resonator structure, the resonator effectively "sees" no anchors at resonance, so is effectively isolated from its surroundings (i.e., from its substrate) and vibrates as if it were virtually levitated, with ideally no path for energy loss to its surroundings.

B. Realizing Exact Quarter-Wavelength Dimensions

Although quarter-wavelength design is seen to maximize Q [24], [27], its ultimate efficacy depends upon device design, and seems to be governed in large

part by the degree to which quarter-wavelength dimensions can be exactly realized. The difficulty in specifying exact dimensions stems from not only the finite tolerances of the lithographic and etching processes used to define a resonator and its supports; but also from mode shape complexities that introduce loss when the support-to-resonator attachment cannot occur at a single point, but rather over a finite length, over which the attachment impedance might be complex and distributed.

For example, the support structure used for an extensional wine-glass mode ring resonator [13], depicted in Fig. 5(b), would ideally attach to the ring resonator at a single point on the radial node line at the ring's outer edge. At this single point attachment, the motion of the ring is mostly rotational, but not entirely, as there is a small tangential component. Although small, this tangential component still presents a path for anchor loss that should be removed if resonator Q is to be maximized. In this case, the simple boundary condition used to design the support beam is not quite appropriate, especially at high frequencies, where the finite attachment width becomes a larger fraction of the acoustic wavelength. As a result, the extensional wine-glass ring resonator of [13] was constrained to Q's <10,000.

On the other hand, the radial-contour mode shape of the spoke-supported ring resonator of this work presents a simpler support-to-resonator attachment interface, where all points at the interface experience only radial movements, as shown in Fig. 2. This means that a spoke support beam anchored at one end and designed to vibrate extensionally, as shown in Fig. 2, with dimensions corresponding to a quarter-wavelength at the frequency of the ring contour-mode resonance, will vibrate so that its free end provides an attachment that presents zero impedance to the ring inner sidewall at all attachment points, i.e., over the full width of the attachment. In other words, the simpler boundary condition of the contour-mode ring of Fig. 2 allows its balanced center-anchored spoke support to present a more ideal free attachment to the ring than tethered outer supports allow at the more complex attachment points of the extensional wine-glass ring of [13], allowing the former to achieve superior Q.

C. Quarter-Wavelength Spoke Support Design

One simple way to specify quarter wavelength spoke support dimensions for the ring of Fig. 1 draws from an understanding of its lumped parameter mechanical equivalent circuit [18]. Fig. 6 presents two equivalent circuit choices: (a) the mobility analogy, in which nodes represent velocities; and (b) the impedance analogy in which nodes represent forces; each for a location at the inner edge of the spoke-supported ring of Fig. 1. These circuits are equivalent duals, and either can be used to model the spoke-supported ring. However, since the present device takes a voltage input to induce an electrode-to-resonator force, it is perhaps more intuitive to interpret nodes as forces as in the impedance analogy. For this reason, the impedance analogy of Fig. 6(b) is used in the following analysis.

In Fig. 6(b), the ring by itself is modeled well by a series mass-spring-damper circuit with element values

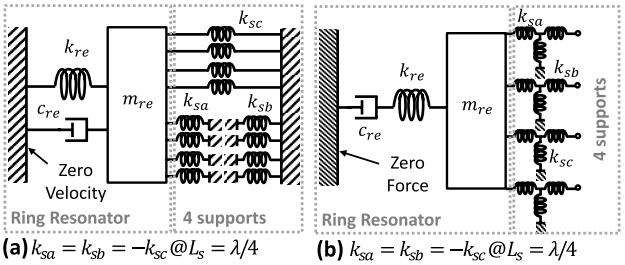

Fig. 6. Equivalent lumped mechanical model for a micromechanical spoke-supported ring resonator (a) using the mobility analogy, in which nodes represent velocities; and (b) using the impedance analogy, in which nodes represent forces.

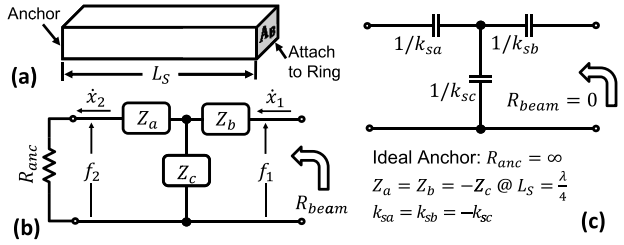

Fig. 7. Equivalent circuits for a support beam. The beam (a) is modeled as a general transmission-line to yield the effective T-network model (b). (c) summarizes the ideal T-network model when beam dimensions satisfy exact quarter wavelength conditions.

specific to the chosen location at the inner edge of the ring. The model for the spoke-supported ring must include circuit branches that represent its four support beams, in this case T-networks of positive and negative springs that model their transmission line behavior at high frequencies. Via straightforward circuit analysis, the resonance frequency of this single degree of freedom mechanical system is easily determined to be

$$f_{om} = \frac{\omega_{om}}{2\pi} = \frac{1}{2\pi}\sqrt{\frac{k_{mre} + 4k_{sc} + 4k_{sa}}{m_{mre}}} \tag{17}$$

where f_{om} is the mechanical resonance frequency without electrical effects, m_{mre} and k_{mre} are equivalent core mechanical mass and stiffness, respectively, of a ring resonator at the support attachment location(s), and where k_{sa} (or k_{sb}) and k_{sc} model the equivalent stiffnesses of the support beams, where all support beams are assumed identical, as is the case in the current work. Eqn. (17) shows that the supports can significantly influence the resonance frequency of a ring if $(k_{sc} + k_{sa})$ is not equal to zero. It follows that if the quantity $(k_{sc} + k_{sa})$ can be set to zero by design, then this dependency disappears, and the ring frequency is as if there were no supports. Quarter-wavelength design is key to achieving this.

To see this, first recognize that the impedance analogy lumped mechanical circuit for each support of Fig. 6(b) reduces to the equivalent circuit of Fig. 7(b), where the springs in the mechanical T-network are simply replaced by impedances Z_a, Z_b, and Z_c. The values of these elements derive from the matrix governing the mechanical impedance

behavior of each support beam as seen by the attached resonator, given by [28]

$$\begin{bmatrix} \dot{x}_1 \\ f_1 \end{bmatrix} = \begin{bmatrix} \cos(\alpha L_S) & jZ_0 \sin(\alpha L_S) \\ \dfrac{j \sin(\alpha L_S)}{Z_0} & \cos(\alpha L_s) \end{bmatrix} \begin{bmatrix} \dot{x}_2 \\ f_2 \end{bmatrix} = \begin{bmatrix} A & B \\ C & D \end{bmatrix} \begin{bmatrix} \dot{x}_2 \\ f_2 \end{bmatrix} \tag{18}$$

where L_S is the beam length, Z_0 is the characteristic mobility $1/(A_B\sqrt{\rho E})$, α is the propagation constant ω_o/v_e, v_e is the velocity $\sqrt{E/\rho}$ of an extensional wave, A_B is the cross section area of the support beam, and $\dot{x}_1$, $\dot{x}_2$, f_1, and f_2 are the velocities and forces at the ends of the support beam.

Equating the circuit of Fig. 7(b) to the chain network described by (18) [5], then solving for the series and shunt impedances in terms of chain matrix elements, yields

$$Z_a = Z_b = \frac{D-1}{B} = \frac{j}{Z_0} \tan\left(\frac{\alpha L_S}{2}\right) \tag{19}$$

$$Z_c = \frac{1}{B} = \frac{-j}{Z_0 \sin(\alpha L_S)} \tag{20}$$

Again, to eliminate support-induced resonance frequency offsets, support beam dimensions should be chosen so that the series and shunt arm impedances of Fig. 7(a) take on equal values and opposite signs at the ring resonance frequency, thereby canceling one another—a condition achieved when the dimensions of each support beam correspond to an effective quarter-wavelength. By inspection of (19) and (20), Z_a and Z_c meet this condition when

$$D = \cos(\alpha L_S) = 0 \tag{21}$$

The solution to (21) yields the L_S's that correspond to effective quarter-wavelengths at the operating frequency. (Note that there are multiple such lengths, allowing a designer to choose the value that works best with the geometry in mind.) With quarter wavelength support dimensions, the impedances of Fig. 7(b) then become

$$Z_a = Z_b = \frac{j}{Z_0} = \frac{k_{sa}}{j\omega} \tag{22}$$

$$Z_c = -\frac{j}{Z_0} = \frac{k_{sc}}{j\omega} \tag{23}$$

In the electrical domain, (22) and (23) correspond to capacitors of value $(1/k_{sa})$ and $(1/k_{sc})$, respectively, and the circuit reduces to the purely electrical form of Fig. 7(c). Analysis of this circuit confirms that the impedance seen looking into the left side is zero, i.e., the support corresponds to a quarter-wavelength, when $k_{sa} = k_{sb} = -k_{sc}$, with stiffnesses governed by

$$k_{sa} = -k_{sc} = \omega_{om} A_B \sqrt{\rho E} \tag{24}$$

where ω_{om} is the radian mechanical resonance frequency of the device defined in Eqn. (17). Ultimately, when quarter-wavelength support dimensions are used, the lumped mechanical circuit model for the spoke-supported ring reduces to that shown in Fig. 7(c), where all supports "cancel" out, leaving the ring itself in a "virtually levitated" state, where it operates as if it has no supports.

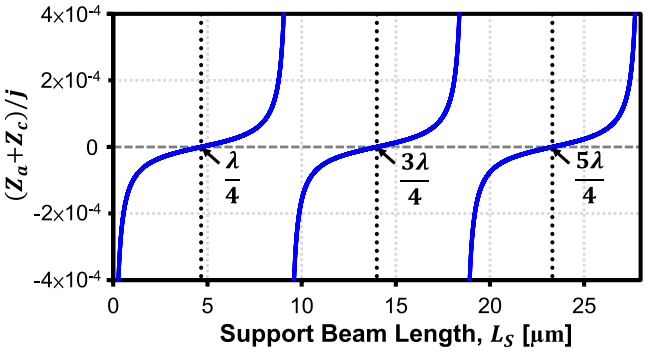

Fig. 8. Effective mechanical impedance, $(Z_a + Z_c)/j$, seen by a 433 MHz ring resonator for a 1 μm-wide, 2 μm-thick polysilicon support beam.

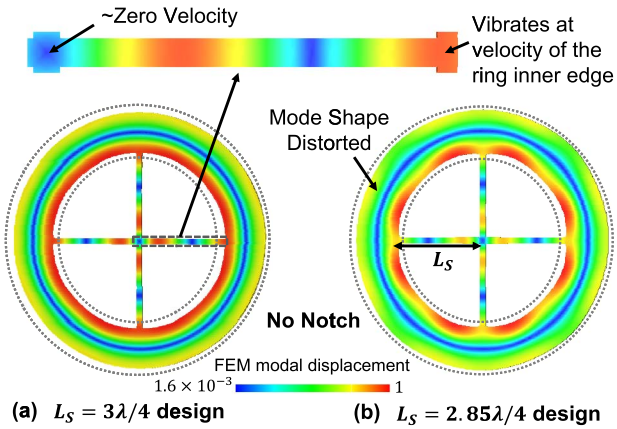

Fig. 9. FEM simulations comparing modal displacements for an un-notched ring when the supports are (a) quarter-wavelength, (b) non-quarter-wavelength.

As an example, Fig. 8 presents plots of the mechanical impedances at 433 MHz for a 1 μm-wide, 2 μm-thick support beam as a function of its length. Here, the impedances Z_a and Z_c are proportional to the mechanical stiffnesses k_{sa} and k_{sc}, respectively, as governed by (22) and (23); while $(Z_a + Z_c)$ is the total effective impedance affecting the resonator system in Fig. 6(b). Once the length of the support beam L_S reaches the values corresponding to single or multiple quarter-wavelengths, this effective impedance (Z_a+Z_c) becomes zero as simulated in Fig. 8 and has (ideally) no effect on the resonator system.

The importance of attaining exact quarter-wavelength supports is perhaps best illustrated by visual comparison of the ring mode shapes achieved when the supports are perfectly quarter-wavelength versus a case where they are slightly off. To illustrate, Fig. 9 presents finite element (FEM) modal analyses on a spoke-supported ring resonator for the case of (a) quarter-wavelength ($3\lambda/4$) support beams for a designed ring resonance frequency, and (b) purposely non quarter-wavelength design ($2.85\lambda/4$). Here, quarter-wavelength design leads to a symmetric and purely radial mode shape shown in Fig. 9(a). In contrast, slight deviation from quarter-wavelength in (b) distorts the ring's radial mode and induces consequent acoustic energy losses to the substrate that lowers the resonator's Q.

If quarter-wavelength supports work by minimizing energy transfer from the ring attachment location on one-side of the

support beam to the anchor on the other, then it makes sense to minimize as much as possible the movement at the ring attachment location. This can be done by attaching the support beam at a node in the resonance mode shape, where ideally there is zero motion. Fig. 1(a) presents a ring design that employs this strategy, for the $n = 2$ mode using a simple notch [15].

D. Practical Spoke-Supported Ring Design

Since quarter-wavelength design constrains the lengths of the support beams to a specific value for the desired ring resonance frequency, the use of centrally-anchored supports in this device forces a sequenced design procedure, where the support structure must be designed first. The design sequence is such that the length of the radial support beams L_S is first set to correspond to one or more (odd numbered) quarter-wavelengths at the desired resonance frequency f_{om}. Use of (21) yields

$$L_S = \frac{n\sqrt{E/\rho}}{4 f_{om}}, \quad n = 1, 3, 5, \ldots \tag{25}$$

where E and ρ are the Young's modulus and density, respectively, of the structural material, f_{om} is defined in Eqn. (17), and n is the odd number of multiple quarter-wavelengths. The value of L_S then sets the inner radius of the ring r_i; i.e., $r_i = L_S$. The outer radius r_o, can now be determined by solving (14).

It should be noted from (14) that the frequency of this device is independent of thickness to first order. As such, filters at many different frequencies, such as required by multi-band and RF channel-select applications, can be achieved in a single fabrication run, with one structural film deposition. This is a distinct advantage over many piezoelectric counterparts (e.g., FBARs) for which frequency is often determined primarily by thickness, making it difficult to manufacture several different multi-band frequencies on the same chip without the need for several structural film depositions, one for each frequency.

V. Lumped Parameter Equivalent Circuits

Given that the spoke-supported ring targets RF frequency control applications, where the device will very likely populate some form of mechanical circuit [6], [18] that in turn must interface with transistor circuits [25], an electrical equivalent model for the device is paramount. Such a model is best derived by first specifying a lumped mechanical equivalent circuit for the spoke-supported ring, then using this to formulate an electrical circuit suitable for simulation using SPICE [29] or other circuit simulators.

A. Lumped Parameter Mechanical Equivalent Circuit

Fig. 6 in Section IV already presented lumped mechanical equivalent circuits in two analogies for a location on the inner edge of the spoke-supported ring. Each circuit comprises a mass-spring-damper that models the core ring resonator structure and either π- or T-networks of springs that model its supports when using the mobility or impedance analogies, respectively. For reasons already mentioned, this work uses the impedance analogy of Fig. 6(b).

Since this lumped circuit attempts to model a device that is actually distributed in nature, the elements of the circuit are location dependent, which means there is a unique equivalent circuit for every specific location on the ring. Regardless of location, the element values will depend fundamentally on the peak total kinetic energy in the vibrating spoke-supported ring, which can be determined for the ring operating in a radial-contour mode by integrating the kinetic energies of all infinitesimal mass elements dm making up the ring to yield

$$KE_{tot} = \frac{1}{2}\int_0^{2\pi}\int_{r_i}^{r_o} dm \times [v(r,\theta)]^2 \tag{26}$$

where $v(r,\theta)$ is the radial velocity magnitude at location (r,θ) given by

$$v(r) = \omega \Re(r) = \omega\,[MJ_1(pr) + NY_1(pr)] \tag{27}$$

Here, ω is the radian frequency of motion, and the infinitesimal mass element takes the form $dm = \rho \times h \times r d\theta \times dr$.

The equivalent mass at position (r,θ) is defined as peak kinetic energy divided by one-half the square of the velocity at that location [28]. Applying this to locations on the inner and outer perimeters of the spoke-supported ring, yields

$$m_{mr}(r_{i,o},\theta) = \frac{KE_{tot}}{0.5\left[v(r_{i,o},\theta)\right]^2} = \frac{\rho h \int_0^{2\pi}\int_{r_i}^{r_o} r\,[\Re(r)]^2\,dr d\theta'}{\left[\Re(r_{i,o},\theta)\right]^2} \tag{28}$$

The equivalent stiffness at a location (r,θ) is simply the product of the equivalent mass at the location and the square of the radian resonance frequency. For locations on inner and outer perimeters, it takes form as:

$$k_{mr}(r_{i,o},\theta) = \omega_{om}^2 m_{mr}(r_{i,o},\theta) \tag{29}$$

To specify an equivalent circuit like that of Fig. 6, a reference point must be chosen that determines the values of the core mass-spring-damper circuit. In the two-port ring resonator of Fig. 1(a), the drive electrodes overlap the ring at its inner perimeter, while the sense electrodes at its outer. Since the desired contour mode-shape here exhibits radial symmetry, any point along the inner or outer edge of the ring can serve as the reference point. Choosing a reference point at the inner edge, the equivalent mass and stiffness for the ring become:

$$m_{mre} = m_{mr}(r_i, 0) \text{ and } k_{mre} = k_{mr}(r_i, 0) \tag{30}$$

Expressions for equivalent damping then readily follow from

$$c_{mre} = \frac{\omega_{om} m_{mre}}{Q} = \frac{k_{mre}}{\omega_{om} Q} = \frac{\sqrt{k_{mre} m_{mre}}}{Q} \tag{31}$$

Since the support attachment locations of Fig. 1(b) are conveniently situated along the inner circumference of the ring, the springs representing the support beams can be directly attached to the mass of the circuit representing the ring. Otherwise, if a support were attached to a location moving at a different velocity from the ring's inner circumference, such as in Fig. 1(a), a velocity transformer would be needed between the ring mass-spring-damper and the coupling beam

T-network to model the difference in velocity, as is commonly done in micromechanical filter design [6], [18].

As an example, for the measured 3-GHz 2nd mode spoke-supported diamond ring of this work with $r_i = 13.8$ μm, $r_o = 16.6$ μm, and $h = 2$ μm, the equivalent stiffness k_{mre} is 0.371 GN/m, which is substantially larger than the 4.5 MN/m posted by previous VHF micromechanical polysilicon disk resonators. Also, note that since the velocities of all points at the inner (and outer) circumference of the ring are independent of θ, determination of the equivalent mass and stiffness of a radial contour mode ring does not require the complex integration needed to obtain accurate model parameters for wine-glass and extensional wine-glass mode resonator counterparts [13], [25].

B. Lumped Parameter Electrical Equivalent Circuit

Having determined the lumped parameter mechanical equivalent circuit for the ring, an electrical equivalent circuit can now be generated to model the action of applied electrical signals that drive the ring into resonance and to predict the magnitudes and phases of the ensuing output currents. To be amenable to circuit simulation via well-established software, this circuit should utilize only electrical elements. Pursuant to this, dualities between the roles of mass, stiffness, and damping, and inductance, capacitance, and resistance, in the respective differential equations governing mechanical and electrical dynamics allow one to equate the different quantities as follows [18]:

$$l_x = m_{mre}; \quad c_x = \frac{1}{k_{mre}}; \quad r_x = c_{mre} \tag{32}$$

where mass, stiffness, and damping values corresponding to input electrode radial locations, i.e., along the inner edge of the ring, are chosen by convention.

There are six electrodes surrounding the ring of Fig. 1, and thus six distinct ports through which to access the device, each of which can serve as an input, an output, or something else, e.g., electrical stiffness-based frequency pulling. A complete model should include the electrical stiffness contributions from each port and be general enough to be independent of whether a port is used for input or output. It should also model the stiffness contributions from the supports described in Section IV, and be general enough to model the effect of attaching them at locations other than the inner ring circumference. In other words, the circuit model must account for the velocity transformation that ensues when attaching supports in this manner.

Fig. 10 presents a lumped parameter electrical equivalent circuit that satisfies all of the above criteria for the spoke-supported ring of Fig. 1. Here, both the electrical-to-mechanical transformations occurring at the electrode-to-resonator capacitive gaps, as well as the velocity transformations occurring between the inner and outer ring edges, are modeled by transformers gauged by their turns ratios.

Transformers also model the velocity transformation between the rings inner edge and the attachment location of the support beams. For the case of Fig. 1, since the T-network-modeled support beams attach to the ring at its inner edge,

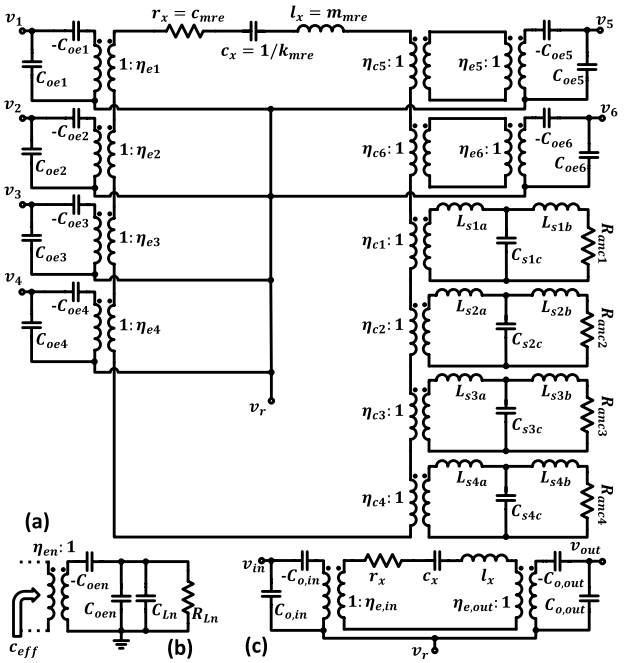

Fig. 10. (a) Complete equivalent circuit model for a spoke-supported ring resonator with four inner (electrodes 1-4) and two outer (electrodes 5-6) electrodes. (b) The load circuit model of a single electrode for the ring resonator. (c) Physically consistent model using actual values of damping, stiffness and mass for elements in a two-port configuration when all input electrodes and output electrodes are connected respectively as shown in Fig. 1(a) and (b).

so are at the same velocity as the lumped *lcr* reference point, the turns ratios of the transformers between the ring and each support beam are simply 1:1. This would not be the case if the supports are attached to the outer ring edge, or at any location other than the inner ring edge.

The turns ratio η_{en} modeling the electromechanical conversion at the nth port results from first considering the functional behavior of an ideal transformer, then inspecting (1) to find

$$\eta_{en} = V_{Pn}\frac{\partial C_{oen}}{\partial r} = \frac{V_{Pn}C_{oen}}{d_o} = V_{Pn}\frac{\varepsilon_o \theta_n h r_{en}}{d_o^2} \tag{33}$$

where h is the ring thickness, C_{oen} and V_{Pn} are the overlap capacitance and dc voltage, respectively, across the nth electrode-to-resonator gap, and θ_n and r_{en} are the subtended angle and radial coordinate location, respectively, of the nth electrode. Note that this coupling factor depends only on the electrode-to-resonator overlap geometry, the dielectric constant of the capacitor, and the voltage applied across it—just as it should.

The turns ratios modeling velocity transformations from the inner disk edge to the outer edge (that occurs between inner and outer electrodes) can be determined with similar reference to an ideal transformer and by inspecting transfer functions specifying the relationship between velocity magnitudes at different locations. For example, the relationship between velocity at a point on the inner ring edge and that at an outer ring edge can be expressed using (27) as

$$\frac{v(r_o)}{v(r_i)} = \frac{\Re(r_o)}{\Re(r_i)} \tag{34}$$

which can also be expressed in terms of equivalent mass or stiffness by

$$\frac{v(r_o)}{v(r_i)} = \pm\frac{\sqrt{KE_{tot}/m_{reo}}}{\sqrt{KE_{tot}/m_{rei}}} = \pm\sqrt{\frac{m_{rei}}{m_{reo}}} = \pm\sqrt{\frac{k_{rei}}{k_{reo}}} \tag{35}$$

where k_{rei} and k_{reo} are the equivalent dynamic stiffnesses that include both mechanical and electrical components, at the inner and outer ring edges, respectively; and m_{rei} and m_{reo} are the corresponding dynamic masses that using (28) simply take the forms $m_{rei} = m_{mr}(r_i, 0)$ and $m_{reo} = m_{mr}(r_o, 0)$, respectively. In the circuit configuration of Fig. 1, the turns ratios for each of the velocity transformers between the ring (referenced at its inner edge) and its (identical) outer electrodes simply become this same ratio:

$$\eta_{c5} = \eta_{c6} = \frac{v(r_o)}{v(r_i)} = \frac{\Re(r_0)}{\Re(r_i)} = \pm\sqrt{\frac{m_{rei}}{m_{reo}}} \tag{36}$$

The 1st contour mode, as shown in Fig. 2(a), produces positive η_{c5} and η_{c6}, as the inner and outer radii moving in concert imply current going into the inner electrodes in phase with current coming out of the outer electrodes (i.e., 0° phase shift). On the other hand, η_{c5} and η_{c6} for the 2nd contour mode (Fig. 2(b)) are negative since the inner and outer ring edges move in opposite radial directions, producing 180° phase-shifted input and output currents.

Finally, static capacitors C_{on} model the physical electrode-to-resonator overlap capacitance at each port n. Note how the bottom terminals of these capacitors all go to a terminal that represents the physical conductive ring structure. In the normal case where the resonant structure is connected to the dc-bias voltage V_P, this terminal in the small-signal equivalent circuit should go to ground. Sometimes, however, an ac signal is applied to the structure terminal to effect mixing for certain applications [30], in which case the terminal in the small-signal circuit should receive the ac source. In either case, one must be careful to include any series resistance present between the ring edge overlapping the electrode and the ultimate point where the dc-bias or ac voltage is applied, as this resistance can heavily influence the performance of devices when used in applications such as filters and oscillators.

C. Electrical Stiffness

During operation, the gap spacing between resonator and electrode changes, which in turn generates a changing electric field, and hence varying electrostatic force in the gap. In a small-signal model, this force is in phase and proportional to disk edge displacement, and thus meets the definition of stiffness. Popularly termed electrical stiffness, this "softens" the equivalent stiffness of the resonator resulting in a negative shift in the resonance frequency [31]. Though often modeled with a simple voltage-dependent change in motional capacitance, c_x, Fig. 10(a) instead models electrical stiffness via "negative" capacitors in series with each of the electrodes that more clearly elucidate the mechanisms behind external load-dependent frequency shifts [32]. For example, when loaded by a complex impedance modeled by C_{Ln} and R_{Ln} in Fig. 10(b), the resultant electrical stiffness generated from each individual electrode-to-resonator gap takes the form

$$k_{en} = -\frac{1}{c_{eff}} = \eta_{en}^2\left[\frac{1}{C_{oen}} - \frac{\omega^2 R_{Ln}^2 (C_{oen} + C_{Ln})}{1 + \omega^2 R_{Ln}^2 (C_{oen} + C_{Ln})^2}\right] \tag{37}$$

where c_{eff} is the effective capacitance seen by the resonator as shown in Fig. 10(b). The electrical stiffness components then perturb the total equivalent stiffness of the resonator to

$$k_{re} = k_{mre} - \sum\nolimits_n k_{en} \tag{38}$$

which in turn yields for resonance frequency

$$f_o = \frac{\omega_o}{2\pi} = f_{om}\sqrt{\left[1 - \sum_n \frac{k_{en}}{k_{mr}(r_{en}, 0)}\right]} \tag{39}$$

where electrical stiffness clearly reduces the resonance frequency from its nominal purely mechanical value. Evaluating (37) with $\omega \approx \omega_{om}$ (valid when mechanical stiffness is much larger than all the electrical stiffnesses combined, as is typically the case here), the maximum electrical stiffness occurs when $R_{Ln} = 0$ (effectively shorting the electrode to ground) in which case k_{en} becomes

$$k_{en,\max} = \frac{\eta_{en}^2}{C_{oen}} = \frac{\varepsilon_o \theta_n h r_{en}}{d_o^3} V_{Pn}^2 \tag{40}$$

recovering the well-known electrical stiffness equation given in [31], valid for cases where the voltage across the electrode-to-resonator gap is kept constant.

If instead of a zero-Ω load, $C_{oen} \gg C_{Ln}$ and $R_{Ln} \to \infty$, the electrical stiffness in (37) approaches zero. In this loading condition, total charge (rather than voltage) remains constant across the electrode-to-resonator gap, resulting in a position-independent electrical field, and thus an absence of electrical stiffness.

D. Reduced Model

The circuit of Fig. 10(a) provides a very general model for the device of Fig. 1, where the ports can be assigned to different purposes at will. In practice specification of port purpose greatly simplifies the equivalent circuit, as shown in Fig. 10(c), which presents the equivalent circuit in Fig. 10(a) corresponding to rings wired as in Fig. 1(a) and (b). Here, the ring in Fig. 1(a) uses all inner electrodes as input and all outer electrodes as output while the ring in Fig. 1(b) splits both inner and outer electrodes in half for use as input and output. The constituent electrodes for each input and output can be combined into one equivalent input electrode and one output electrode, with electromechanical coupling factors modified as

$$\begin{aligned} \eta_{e,in} &= \eta_{e1} + \eta_{e2} + \eta_{e3} + \eta_{e4} \\ \eta_{e,out} &= |\eta_{c5}|\eta_{e5} + |\eta_{c6}|\eta_{e6} \end{aligned} \tag{41}$$

for Fig. 1(a); and

$$\begin{aligned} \eta_{e,in} &= \eta_{e1} + \eta_{e2} + |\eta_{c5}|\eta_{e5} \\ \eta_{e,out} &= \eta_{e3} + \eta_{e4} + |\eta_{c6}|\eta_{e6} \end{aligned} \tag{42}$$

for Fig. 1(b), where η_{e1} to η_{e6} are defined in (33) while η_{c5} and η_{c6} are defined in (36). The equivalent input and output electrode-to-resonator overlap capacitors become

$$\begin{aligned} C_{o,in} &= C_{oe1} + C_{oe2} + C_{oe3} + C_{oe4} \\ C_{o,out} &= C_{oe5} + C_{oe6} \end{aligned} \tag{43}$$

for Fig. 1(a); and

$$\begin{aligned} C_{o,in} &= C_{oe1} + C_{oe2} + C_{oe5} \\ C_{o,out} &= C_{oe3} + C_{oe4} + C_{oe6} \end{aligned} \tag{44}$$

for Fig. 1(b).

The circuits of Fig. 10(a) or (c) are the most useful for electromechanical design, since they support more general I/O port configurations, and they fully model all relevant design aspects of the spoke-supported ring resonator, from the amount of electrode-to-resonator overlap and gap spacing needed to attain a given coupling factor, to the impact that slight deviations from quarter-wavelength of the couplers have on resonance frequency and Q, to the degree to which external elements affect electrical stiffness and in turn impact the resonance frequency. However, for comparison with other tank circuits, e.g., quartz crystals, equivalent electrical *LCR* circuit elements are sometimes desirable. The expressions for the equivalent electrical elements result from merely reflecting the circuit of Fig. 10(c) through the leftmost transformer with all outputs grounded. Doing so yields

$$R_x = \frac{\sqrt{k_{re} m_{mre}}}{Q \eta_{e,in} \eta_{e,out}}; \quad L_x = \frac{m_{mre}}{\eta_{e,in} \eta_{e,out}}; \quad C_x = \frac{\eta_{e,in} \eta_{e,out}}{k_{re}} \tag{45}$$

Using (45), the expression for the electromechanical coupling factor (C_x/C_o) at port 1, which effectively equals the popular k^2_{eff} at low values, takes the form for the 2nd contour mode:

$$(C_x/C_o) \approx \frac{\varepsilon_o \theta_1}{2\pi^3 \Lambda (1 + r_o/r_i)} \cdot \frac{V_{P1}^2}{d_o^3 f_o \sqrt{E \cdot \rho}} \tag{46}$$

where Λ relates the static mass of the ring to its dynamic mass and depends on the mode shape function (11). From (46), (C_x/C_o) depends most heavily on bias voltage, V_{P1}, and electrode-resonator gap, d_o, where the latter shows a strong third power dependence. In fact, a 10× increase in dc-bias V_{P1} and a similar decrease in gap spacing d_o yields a 5 order of magnitude increase in (C_x/C_o), giving an indication of just how adjustable this parameter is, given a capable technology. Note also the importance of Young's modulus E and density ρ, where materials with smaller $E \cdot \rho$ products yield better (C_x/C_o). For example, polysilicon's $E \cdot \rho$ of 3.45×10^{14} Pa $\cdot$ kg/m^3 is 12 times smaller than the 4.19×10^{15} Pa $\cdot$ kg/m^3 of diamond, which yields a 3.5 times better (C_x/C_o) for designs using the same frequency, gap spacing, and bias voltage.

VI. Experimental Results

Fig. 11 presents cross-sections of the fabrication process that achieves the spoke-supported ring resonators of this work with strong, perfectly-centered, self-aligned peg anchors.

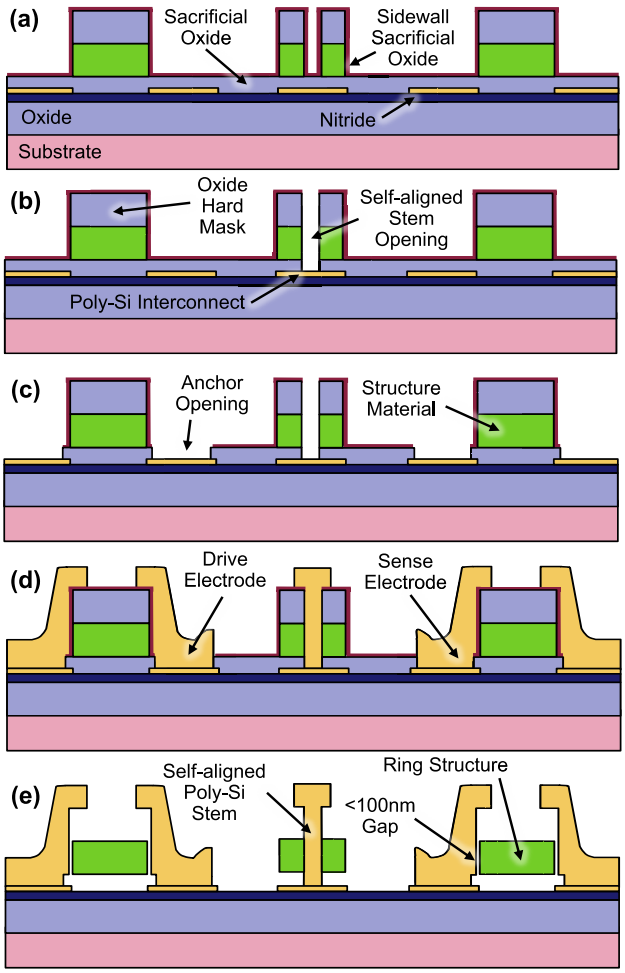

Fig. 11. Fabrication process flow for polysilicon and microcrystalline diamond ring resonators. (a)-(d) illustrate the resonator construction through repeated LPCVD film depositions, lithography, and plasma etches, followed by a 49% HF wet etch process to remove the sacrificial oxide to yield the final released structure of (e).

The process borrows heavily from [12] and [23] and starts with a heavy phosphorous diffusion via $POCl_3$ to serve as the substrate ground plane, followed by sequential depositions of 2 μm of high temperature LPCVD oxide (HTO) at 950°C and 350 nm of stoichiometric silicon nitride at 800°C together serve to isolate devices and interconnects from the conductive silicon substrate. Next, vias (not shown) are lithographically defined to delineate substrate ground contacts and etched through the nitride and oxide down to the substrate ground plane. Interconnect polysilicon is then deposited at 588°C to a thickness of 350 nm and doped, again via $POCl_3$. After patterning this polysilicon layer to form substrate ground contacts, ground planes, and interconnects, 650 nm of HTO is deposited to act as a sacrificial layer to temporarily support the subsequent structural layer during its deposition and patterning. The 2 μm-thick structural film—either $POCl_3$-doped polysilicon at 588°C or hot-filament boron-doped CVD microcrystalline diamond at 730°C [23]—is then deposited and capped with a 1.2 μm-thick film of HTO that serves as both a hard mask during etching of the structural film, and later as a spacer layer to separate the ring from overhanging electrode portions. The composite oxide

mask-structural film layer is patterned in a *single* mask to define not only the ring structure, but also the 2 μm-diameter opening at its center that defines the eventual location of the peg support, as shown in Fig. 11(a). Definition of the peg support location via the same mask as the resonant structure self-aligns the peg to the very center of the ring structure, which is paramount to maximizing anchor rigidity.

An HTO deposition less than 100 nm-thick that conformally coats all surfaces, including structure sidewalls, then defines the ever-important electrode-to-resonator gap spacing. Since this thin oxide film also coats the stem opening, *cf.* Fig. 11(a), steps are needed to remove it in the stem before stem-refilling to permit electrical contact between the ring support structure and the stem. This is done by spinning a thick photoresist and patterning it to expose the stem and the electrode vias, after which a combination of dry and wet etching removes the sidewall sacrificial spacer oxide in the stem opening (*cf.* Fig. 11(b)) and the underlying bottom sacrificial oxide down to interconnect on the substrate, as shown in Fig. 11(c). A subsequent 2 μm polysilicon deposition then not only provides the material for electrodes, but also refills the anchor vias to create very rigid, self-aligned, electrically-contacted stems. This last polysilicon layer is then doped and patterned as shown in Fig. 11(d) to define the electrodes and stem tops. Finally, structures are released in 48.8 wt. % HF to yield the final cross-section of Fig. 11(e).

A. Measurement Setup

A custom-built vacuum chamber enabled characterization of the polysilicon structural material resonators at the mtorr or lower pressures needed to remove viscous gas damping. In this apparatus, dies containing devices-under-test were epoxied to a custom-built printed circuit board (PCB) chip carrier containing isolated ports that connect to on-die devices via bondwires then direct signals through vacuum chamber feedthroughs to external measurement instrumentation. Additionally, a Lakeshore FWPX vacuum probe station allowed rapid measurement of the very high frequency diamond structural material resonators without the need for wirebonding, which facilitates testing of a large number of device variations. For all vacuum measurements, a turbo molecular pump evacuated the chamber to pressures on the order of 10 μtorr before testing.

Frequency response measurements were taken using an Agilent E5071B network analyzer using the measurement scheme of Fig. 12, where the network analyzer produces an ac drive signal on one port and measures power output on a second port to a 50 Ω load. Beyond measurement instrument hookups, Fig. 12(a) depicts the parasitic capacitive signal path through the substrate layers underlying a ring device. Though not a significant problem at low frequencies, the signal feeding through this path becomes larger as frequencies rise to the GHz range, where it can mask or distort a device's output current, making it difficult to determine important parameters, like Q.

To prevent inaccurate measurement due to feedthrough, this work employs the mixing measurement [30] setup, shown in Fig. 12(b), that separates motional and feedthrough currents

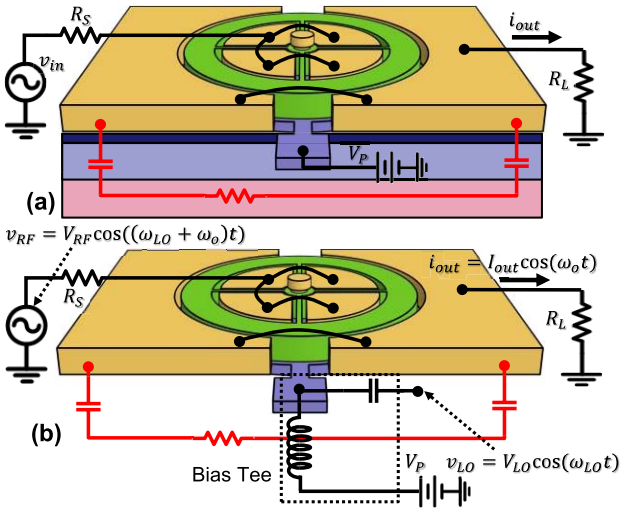

Fig. 12. Schematics comparing (a) a typical two-port measurement scheme and (b) the mixing measurement scheme used here to bypass the parasitic feedthrough path for the fabricated devices. In both cases, measurements employ a network analyzer with $R_S = R_L = 50\ \Omega$.

in the frequency domain, thereby allowing measurement of motional current without interference. As shown, this setup uses a bias tee to add a 1-2MHz local oscillator (LO) signal to the dc-bias voltage already applied to the conductive resonator structure. The network analyzer then sources an RF signal at a frequency higher than the expected resonance frequency by the frequency of the LO signal while measuring at resonance.

Even though none of the applied signals are at the resonance frequency, f_o, they still generate a mechanical force at resonance via the square-law voltage-to-force transfer function of the input capacitive transducer, where

$$F_{in} = \frac{1}{2}\frac{\partial C_{o,in}}{\partial r}\left[V_P + V_{LO}\cos(\omega_{LO}t) - V_{RF}\cos(\omega_{RF}t)\right]^2$$

$$\begin{aligned} F_{in} = \frac{1}{2}\frac{\partial C_{o,in}}{\partial r}\big[&V_P^2 + (V_{LO}\cos(\omega_{LO}t))^2 \\ &+ (V_{RF}\cos(\omega_{RF}t))^2 \\ &- V_{LO}V_{RF}\left(\cos\left((\omega_{LO} + \omega_{RF})\,t\right)\right. \\ &\left. + \cos\left((\omega_{LO} - \omega_{RF})\,t\right)\right) + \ldots\big] \end{aligned} \tag{47}$$

Here, multiplication of the LO and RF signals produces sum and difference terms. If frequencies are chosen such that $\omega_{RF} - \omega_{LO} = \omega_o$, a force arises at the resonance frequency:

$$\begin{aligned} F_{in}@\omega_o &= \frac{1}{2}\cdot\frac{\partial C_{o,in}}{\partial r}V_{LO}\cdot V_{RF}\cdot\cos\left((\omega_{RF} - \omega_{LO})\,t\right) \\ \rightarrow F_{in}@\omega_o &= \frac{1}{2}\cdot\frac{\partial C_{o,in}}{\partial r}\cdot V_{LO}\cdot V_{RF}\cdot\cos\left(\omega_o t\right) \end{aligned} \tag{48}$$

The ensuing motion then combines with the resonator bias voltage, V_P, to produce an output current at ω_o. Note that none of the applied signals are at the resonance frequency of the ring under test, so none can introduce feedthrough at this frequency. As long as the signal is measured within only a narrow frequency band, as is the case when a network analyzer senses the resonator output, parasitic feedthrough currents at frequencies different from the motional current will not interfere, allowing accurate measurement of the resonator response alone.

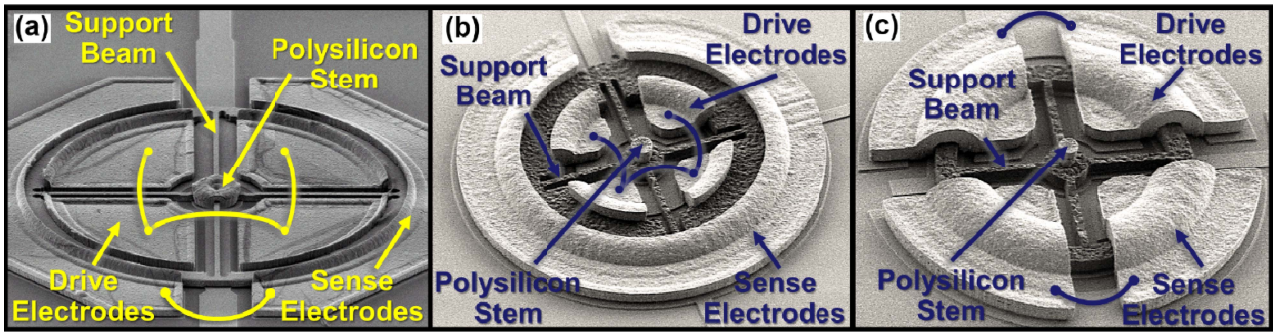

Fig. 13. SEM's of fabricated ring resonators: (a) A 2nd-mode 422-MHz polysilicon ring with polysilicon stem; (b) a 2nd-mode 900-MHz diamond ring with polysilicon stem using electrode configuration B; and (c) a 2nd-mode 3-GHz diamond ring with polysilicon stem using electrode configuration A.

Note that the value of dc-bias voltage V_P is practically limited by the pull-in voltage V_{PI} at which electrode-to-resonator electrostatic forces pull the ring into one or more of its electrodes. If the devices of this work truly looked like those depicted in Fig. 1, with ring and electrode tops flat and aligned, then permissible voltages might have been as high as the 60 V demonstrated in [33] on much lower frequency wine-glass disk devices. However, as shown in Fig. 11(e), the fabrication process does not include the final planarization step used in [33], so portions of the electrodes of devices overhang the rings. Finite element analysis shows that these overhangs significantly compromise the maximum permissible value of V_P by creating a condition where a ring pulls up into its electrode overhangs at a voltage much smaller than the expected lateral resonator-to-electrode pull-in voltage. In this work, electrode overhangs effectively limit permissible V_P's to around 8V, which in turn made measurement challenging, even when mixing.

B. Resonator Measurements

Several self-aligned, radial-contour mode micromechanical spoke-supported ring resonators with frequencies from 24 MHz to 2.97 GHz were designed in polysilicon and diamond structural materials, then fabricated using the process flow of Fig. 11. Fig. 13(a) presents the SEM of one such fabricated polysilicon structural material device constituting a 433-MHz 2nd mode spoke-supported ring. Fig. 13(b)-(c) present similar ring devices in diamond structural material fabricated in a parallel process and designed to resonate in the 2nd-mode at 900-MHz and 2.97-GHz, respectively. The set of fabricated designs feature both notched and un-notched supports for comparative purposes. In addition, an ensemble of 900-MHz diamond devices were fabricated with varying support beam lengths in 50 nm steps in order to map out resonator performance due to deviations from perfect quarter-wavelength operation. Table 1 summarizes the dimensions used for each design along with measured and predicted performance data.

Although previous work demonstrated that Q's $>$10,000 in air are possible for UHF μmechanical resonators [14], all devices of this work were measured in vacuum in order to isolate the anchor loss mechanisms that the subject suspension designs intend to alleviate. Fig. 14(a)-(b) present two-port

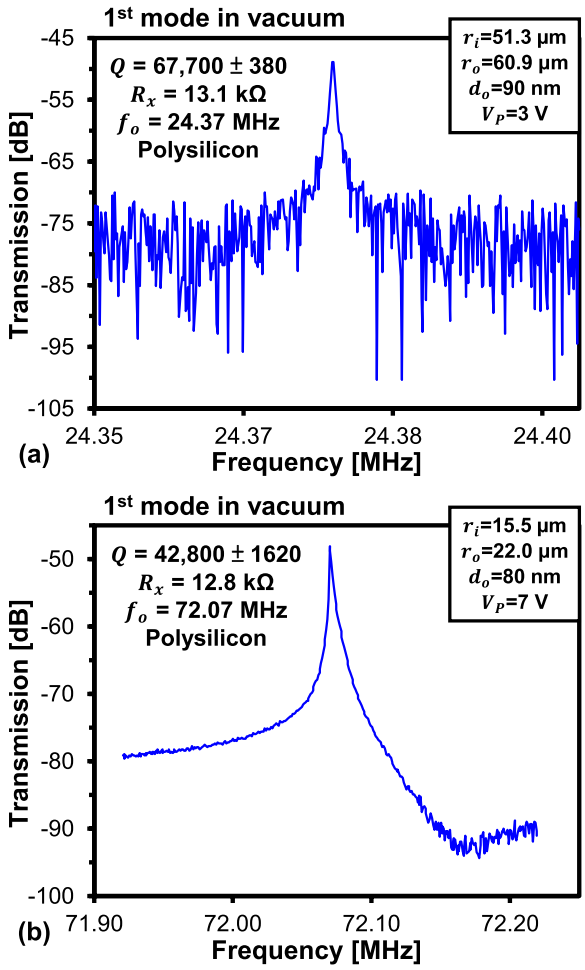

Fig. 14. Measured frequency characteristics for fabricated HF to VHF micromechanical spoke-supported ring resonators using a two-port measurement set-up under vacuum. (a) 1st mode 24.37 MHz spoke-supported ring with direct support attachments, using a very small bias voltage of 3 V. (b) 1st mode 72.07 MHz spoke-supported ring with direct support attachments, using a $V_P = 7$ V.

direct-measured frequency characteristics for un-notched spoke-supported polysilicon ring resonators vibrating in vacuum in the first contour-mode of Fig. 2(a), with bias voltages of 3 V and 7 V, and center frequencies of 24.37 MHz and 72.07 MHz, showing Q's of 67,700 and 42,800, respectively. The very high Q of 67,519 at HF contributes

TABLE I
SPOKE-SUPPORTED RING RESONATOR DESIGN AND PERFORMANCE SUMMARY

Parameter	Source	Operating Frequency					Unit
		*24.4 MHz**	*72.1 MHz**	*422 MHz*	*900 MHz*	*3 GHz*	
Design/Given							
Structure Material	-	Polysilicon	Polysilicon	Polysilicon	Diamond	Diamond	-
Inner radius, r_i	layout	51.3	15.5	23.3	19.4	13.8	μm
Outer radius, r_o	layout	60.9	22.0	33.0	29.1	16.6	μm
Thickness, h	layout	2.0	2.0	2.0	2.0	2.0	μm
Electrode-to-resonator gap, d_o	measured	90	80	90	75	75	nm
Density, ρ	[23]	2300	2300	2300	3500	3500	kg/m^3
Young's modulus, E	[23], [34]	150	150	150	1198	1198	GPa
Poisson ratio, σ	[23]	0.226	0.226	0.226	0.07	0.07	-
RF input amplitude, v_{RF}	measured	-	-	0.178	2	2	V
LO carrier amplitude, v_{LO}	measured	-	-	6	1.12	2	V
DC-biased voltage, V_P	measured	3	7	7	6	8	V
Resonator mass, m_{mre}	Eqn. (30)	1.55×10^{-11}	3.50×10^{-12}	3.90×10^{-12}	4.18×10^{-12}	8.52×10^{-13}	kg
Resonator stiffness, k_{mre}	Eqn. (30)	3.23×10^{5}	6.61×10^{5}	2.86×10^{7}	1.55×10^{8}	3.71×10^{8}	N/m
Damping factor, c_{mre}	Eqn. (31)	3.32×10^{-8}	3.45×10^{-8}	1.00×10^{-6}	3.29×10^{-7}	4.44×10^{-7}	kg/s
Inner-to-outer coupling ratio $\eta_c = \eta_{c5} = \eta_{c6}$	Eqn. (41)(42)	0.963	0.930	-0.839	-0.816	-0.912	-
Electromech. coupling, $\eta_{e,in}$	Eqn. (41)(42)	1.37×10^{-6}	1.23×10^{-6}	1.46×10^{-6}	1.77×10^{-6}	1.81×10^{-6}	C/m
Electromech. coupling, $\eta_{e,out}$	Eqn. (41)(42)	1.81×10^{-6}	1.87×10^{-6}	2.00×10^{-6}	2.71×10^{-6}	1.81×10^{-6}	C/m
Static Overlap Capacitance, $C_{o,in}$	Eqn. (43)(44)	4.12×10^{-14}	1.40×10^{-14}	1.87×10^{-14}	2.21×10^{-14}	1.78×10^{-14}	F
Static Overlap Capacitance, $C_{o,out}$	Eqn. (43)(44)	5.65×10^{-14}	2.29×10^{-14}	3.06×10^{-14}	4.15×10^{-14}	1.78×10^{-14}	F
Performance							
Quality factor in vacuum, Q	measured	67,700	42,800	10,000	77,200	42,900	-
Resonant frequency, f_o	measured	24.4	72.1	422.0	899.6	2970	MHz
	Eqn.(39)	23.0	69.2	430.8	969	3321	
Series resistance, R_x	measured	13.2	13.6	297.8	51	81	kΩ
	Eqn. (45)	12.5	13.7	281.9	69	136	
Inductance, L_x	Eqn. (45)	5.857	1.385	1.099	0.873	0.261	H
Capacitance, C_x	Eqn. (45)	8.20×10^{-18}	3.82×10^{-18}	1.24×10^{-19}	3.09×10^{-20}	8.79×10^{-21}	F
Coupling Efficiency, $C_x/C_{o,in}$	calculated	0.0194 %	0.0266 %	6.47×10^{-4} %	1.4×10^{-4} %	4.94×10^{-5} %	-
Coupling Efficiency, $C_x/C_{o,out}$	calculated	0.0142 %	0.0162 %	3.96×10^{-4} %	7.44×10^{-5} %	4.94×10^{-5} %	-

*Direct two-port measurement.

to the low series motional resistance of this resonator, which is only 13.1 kΩ with $V_P = 3$ V. (A 10× higher bias voltage of 30 V, if permissible, would yield a 100× smaller R_x of 131 Ω.) Moreover, the average radius of the device measured in Fig. 14(a) is 3× larger than that of Fig. 14(b), which as predicted in Section V, allows the former to achieve a similar R_x, despite the use of a smaller V_P.

Fig. 15 presents the frequency response of another polysilicon resonator dimensioned to operate at 422 MHz in its 2nd mode using the notched support design and measured using the mixing measurement setup of Fig. 12(b), with the network analyzer operated in "offset frequency" mode, where the output signal is measured at a user-selectable frequency offset equal to the RF drive frequency minus the LO frequency. The resultant frequency characteristics of Fig. 15 allows accurate extraction of the true resonator response and measurement of the Q of 10,000.

Fig. 16 presents the frequency response of a similar ring design fabricated in microcrystalline diamond. The low-loss and high acoustic velocity of the diamond material increases the frequency of the 2nd mode to 900 MHz while simultaneously boosting Q to an exceptional 77,200. Reducing ring width further, the resonator operating frequency increases to 2.97 GHz in Fig. 17, while still retaining a remarkable series resonant Q of 42,900—a record high at these frequencies. The 8-10% decrease in frequency of these devices as compared with prediction, *cf.* Table 1, likely results from slight differences in the material properties of the diamond used here compared with [23].

The frequency response data demonstrate operation at the designed mode frequency for these ring resonators. However, these resonators display many additional unwanted mechanical modes that can interfere with desired operation in real-world applications. Fortunately, lateral and symmetric placement of electrodes suppresses electrical detection of the out-of-plane spurious modes and of the modes that do not match the electrode symmetry. Despite this, two primary symmetric resonances near the 2nd mode frequency remain observable.

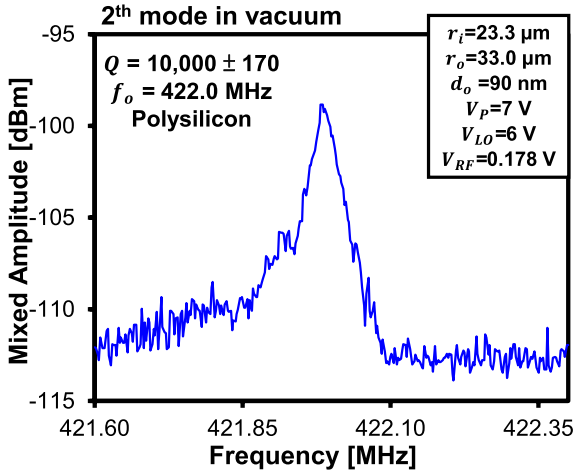

Fig. 15. Measured frequency characteristic using a mixing measurement set-up under vacuum for a 2nd mode 422-MHz polysilicon spoke-supported ring with polysilicon stem and notched support attachments.

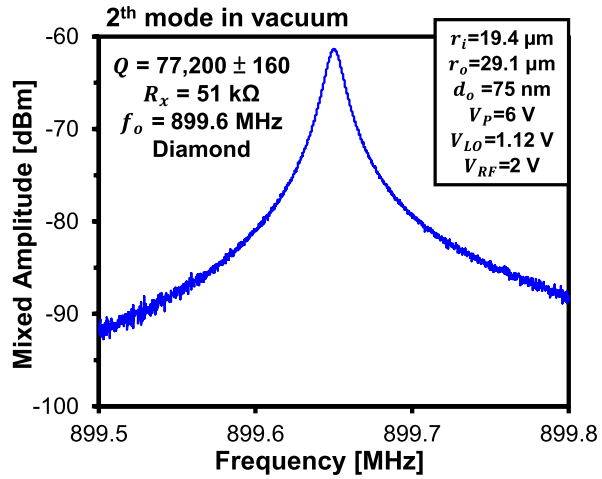

Fig. 16. Mixing-measured frequency response of a 2nd mode 900-MHz diamond spoke-supported ring with polysilicon stem.

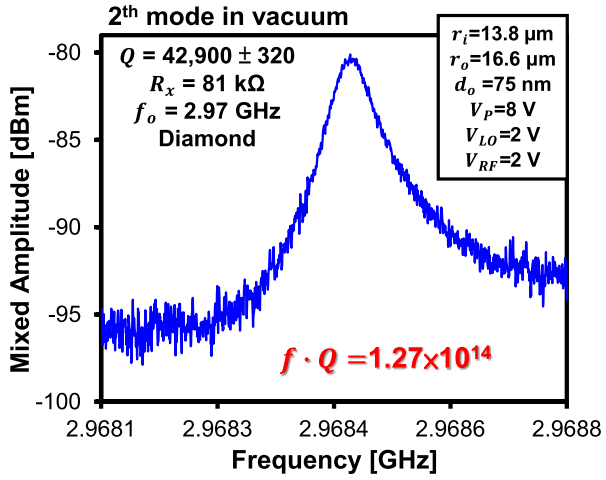

Fig. 17. Mixing-measured frequency response of a 2nd mode 2.97-GHz ring demonstrating the highest to-date $f \cdot Q$ product of 1.27×10^{14}.

Fig. 18 presents measured frequency data for the designed mode as well as the measured spurious mode for a large ensemble of 900-MHz 2nd mode diamond rings with varying

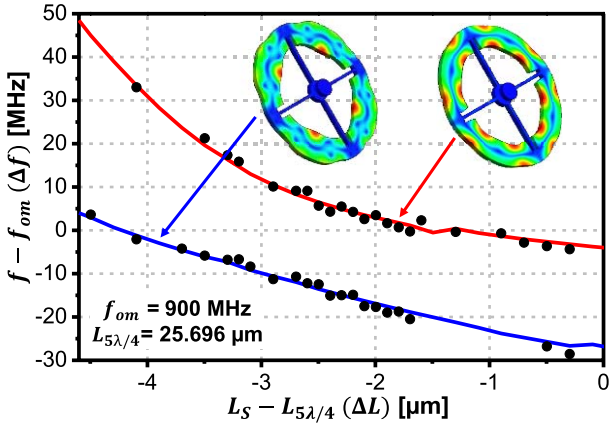

Fig. 18. Measured frequency response (black dots) of the two strongest modes of several 900-MHz ring resonators as their support beam lengths deviate from quarter-wavelength. The data matches well the FEM-simulated blue and red curves.

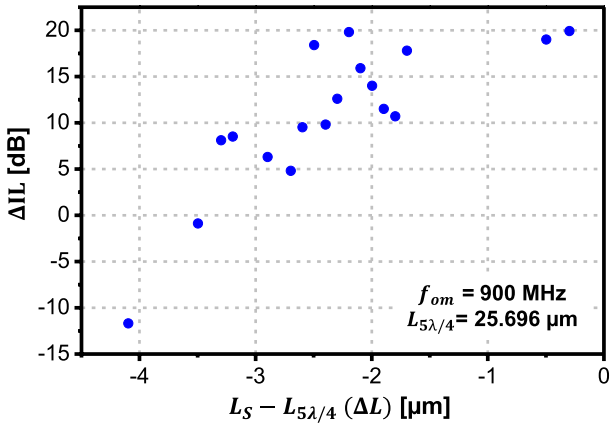

Fig. 19. Measured difference in resonator insertion loss (blue dots) of the two strongly coupled modes shown in Fig. 18 as support beam length changes. When the beam length approaches $\lambda/4$, the ring is virtually "levitated", so behaves as if it had no supports. This enhances its motional amplitude and lowers its insertion loss, all while suppressing the 2nd hybrid mode.

support beam lengths expressed as deviations from quarter-wavelength. Black dots plot out measured frequencies of the two resonator modes most coupled by the electrode geometry, corresponding to the desired 2nd ring mode (top curve) as well as an additional hybrid mode (bottom curve). This reveals a clear trend as support beam lengths deviate from perfect quarter-wavelength, where the desired mode begins to deviate significantly from the target frequency when support beams deviate by more than 2 μm from quarter-wavelength. Overlaid blue and red curves represent calculated frequencies from FEM simulation showing excellent agreement with measured data.

Changes in support beam length further affect loading of the mechanical mode, where mode shape distortion ensues when the vibrating ring sees non-zero impedances from the supports, as illustrated in the simulations of Fig. 18. Here, the amount of loading depends on the deviation of support beam length from the $\lambda/4$ condition described in Section IV needed to present an effective zero impedance to the inner

ring edge. Fig. 19 presents the difference in insertion loss in two-port network analyzer measurements of the two dominant modes in the 900 MHz ring resonators as support beam length changes. Note that measurement of this insertion loss provides a direct gauge of support beam loading changes independent of intrinsic loss variations among the many devices measured.

The observed difference in relative coupling of the two measured modes of greater than 30 dB as beam length is swept confirms the dependence of support beam loading on beam length deviations from the optimal $\lambda/4$ condition. Here, the correctly designed support length provides 20 dB suppression of the undesired hybrid mode, which is sufficient for many oscillator and filter applications. This not only emphasizes the importance of proper design to maximize resonator Q, but also offers the potential to enhance the designed mode while further suppressing undesired spurious modes.

C. Remarks on Q

Although the above experiments are unable to precisely decipher the individual contributions of different loss mechanisms to the measured Q's, they lend some qualitative insight. For example, that diamond material yields a much higher $f \cdot Q$ product than polysilicon in an identical structure vibrating in its second contour mode confirms the efficacy by which the centralized, symmetric, quarter-wavelength spoke-support system suppresses anchor loss. Indeed, it seems to suppress anchor loss well enough to make it secondary to intrinsic material loss in determining the ultimate Q of second contour mode polysilicon resonators.

The low Q's observed for second contour-mode polysilicon rings when compared with diamond also suggest the intrinsic loss of their structural materials as the dominant loss mechanism. Firm conclusions are elusive, however, and will likely require further dedicated study to isolate all potential loss mechanisms.

D. Device Design Insights

While the motional impedances here of tens of kΩ at GHz are sufficient for many sensor applications, use of these devices in oscillators or filters motivates reduction of R_x to under 1 kΩ. Inspection of equations (33) and (45) indicate that the capacitive gap offers the most straightforward path towards reduced R_x, which is inversely proportional to the fourth power of gap size. The dc-bias voltage V_P also provides a very strong knob, with a square-law dependence, although its value is often limited by power supply or pull-in limitations, as described in Section VI.A. Mechanically-coupled arrays of resonators allow further reduction in R_x without a significant reduction in Q [7], [35]. As illustration, an example design suitable for oscillator construction might use modest 30 nm gaps with a coupled array of seven 3-GHz diamond rings to achieve a motional resistance of 300 Ω with a V_P of only 8 V, all within the capabilities of demonstrated fabrication technology [7]. Arguably, if R_x were the only consideration, then there would be little concern, since attaining a given R_x is a matter of achieving the needed electrode overlap area, be it via arraying or some other method. Unfortunately, R_x is not the only concern; rather, electromechanical coupling, as gauged by (C_x/C_o), is often more important.

In particular, for filter applications, there are two regimes to consider: 1) narrow bandwidth filters such as the tiny 0.03% bandwidth required for direct RF channel-selection [4] and 2) wide bandwidth filters covering bandwidths larger than 0.1% and suitable for full band selection. For narrowband operation, insertion loss becomes a primary concern [6], [36], so resonator Q is of utmost importance, where high values of Q minimize insertion loss. Meanwhile, electromechanical coupling (C_x/C_o) is less important [36], with required values proportional to the filter percent bandwidth, which is small for the case of channel-selection. Thus, for channel-selection, resonators using diamond structural materials are preferred as they have higher Q than polysilicon counterparts. In addition, materials with higher acoustic velocity (such as diamond) enable higher frequencies with larger resonator dimensions, which in turn relaxes fabrication tolerances. For a 3-GHz resonator design, for example, the width of the ring is approximately 3 μm in diamond while only 1.4 μm in polysilicon.

In contrast, for wide bandwidth filter applications, the limiting factor is the electromechanical coupling (C_x/C_o), defined in Eqn. (46). This term sets limits on the ability to terminate a given filter bandwidth without undue passband distortion, where again, (C_x/C_o) must be at least comparable to the % bandwidth [5]. To this end, resonator technologies such as FBAR [37] and CMR [38] post (C_x/C_o) values as high as 7% and 2%, respectively, making them good candidates for band-select applications where the comparatively low Q of these options does not limit performance.

Note how it is not enough for a resonator to merely have a large $(C_x/C_o)-Q$ product (or equivalently, k_{eff}^2-Q product). Indeed, FBAR resonators that routinely post $(C_x/C_o) - Q$ products over 100 are not suitable for channel-select filter design despite their large (C_x/C_o), since they lack the needed Q to attain reasonable insertion loss. Ultimately, $(C_x/C_o)-Q$ is not an appropriate metric to gauge the efficacy of a given resonator type in a given filter; rather, specific knowledge of Q and coupling is needed, where Q is paramount for channel-selection, while coupling is more important for band-selection. Recognizing this, reference [36] dispenses with $(C_x/C_o) - Q$ (or $k_{eff}^2 - Q$) product as a metric and instead gauges the suitability for RF-channel-selection of numerous non-overmoded resonators via a plot of both Q and (C_x/C_o) alongside needed values for a sensible channel-selecting filter bank plan. In this plot ([36, Fig. 21]), although the Q of the diamond ring resonator of Fig. 17 exceeds the needed value at 3 GHz, its 0.00005% (C_x/C_o) is well short of the needed 0.03%. In other words, like all resonators in the plot except one using capacitive-piezoelectric resonator technology [39], the diamond ring resonator of this work still does not completely satisfy the needs of an RF channel-selecting filter at 3 GHz.

By inspection of (46), (C_x/C_o) of the ring resonator increases quickly with decreasing gap spacing d_o or increasing dc-bias voltage V_P, but decreases with increasing resonance frequency. From a design perspective, reducing gap spacing offers the fastest path to increasing (C_x/C_o).

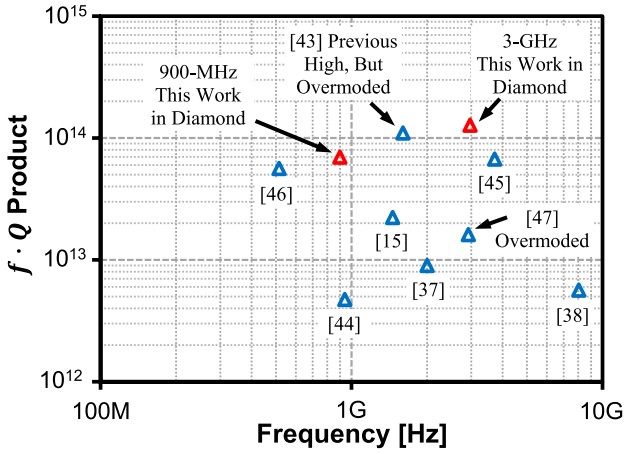

Fig. 20. The $f \cdot Q$ products of previously published high $f \cdot Q$ acoustic resonators along with those of this paper.

Akgul and Nguyen [7] have already demonstrated gap spacings of 40 nm using a similar sacrificial sidewall spacer layer to that used here, only thinner. This, together with gap-filling strategies like that of [40], provide some confidence that 30 nm gaps and below are probably within reach of planar technologies. Perhaps more challenging than attaining the actual gaps will be control of stresses that might more easily push structures across the much smaller gaps into their electrodes.

Assuming these challenges can be overcome, decreasing gap size from the typical 80 nm used here to 10 nm improves (C_x/C_o) by 512 times. For the 3-GHz diamond resonator, this 10 nm gap corresponds to a (C_x/C_o) of approximately 0.08% with V_P of 15 V, while an equivalent polysilicon device with $(E \cdot \rho)$ product of 1/12 that of diamond has (C_x/C_o) of 0.28%. If other materials are considered, additional improvement is available through material properties. Aluminum, for example, has an exceptional $(E \cdot \rho)$ product, 22 times smaller than diamond's, and would yield a (C_x/C_o) of 0.37% with the same V_P and gap. To achieve 3-GHz operation, however, aluminum's small acoustic velocity necessitates a design width of only 0.9 um, which introduces additional process challenges. As a general rule of thumb for GHz capacitive-gap resonators, it is desirable to use a material that has, in addition to low material loss, high acoustic velocity $\sqrt{E/\rho}$ and small $(E \cdot \rho)$ product.

VII. Conclusions

The demonstrated frequency range from 10's of MHz up to 3 GHz of the described spoke-supported ring resonators illustrates clearly the efficacy by which simple Computer-Aided Design (CAD) provides frequencies for a wide range of applications, from HF reference oscillators, to VHF and UHF filters. The complete theoretical framework presented for the design and analysis of such resonators further facilitates their use in potential LSI or VLSI designs, while highlighting the innovations required to achieve frequencies and Q's suitable for use in RF channel-select filters. In addition, the use of equivalent circuit models to help circuit designers visualize the mechanical operation of these resonators hopefully encourages the use of these devices in larger circuits or systems.

While the Q at 3 GHz is accompanied by an electromechanical coupling insufficient for a reasonable channel-select filter bank plan [36], this deficiency should be fixable via reductions in electrode-to-resonator gaps to values not much smaller than already achieved for other capacitive-gap transduced devices [7], [40]. Work towards this is ongoing that if successful stands to produce channel-select filters with tuned passband precision like that of [7], but at frequencies in the GHz range.

Regardless, the record high Q of 42,900 at 2.97 GHz for the microcrystalline diamond device measured under vacuum corresponds to a frequency-Q product of 1.27×10^{14}, which is the highest measured value yet seen for micromechanical resonators at room temperature, and compares favorably even with devices measured under cryogenic conditions [41], [42]. Comparison with previous high frequency-Q product room temperature acoustic resonators [15], [37], [38], [43]–[47] in Fig. 20 reveals that the result of this work exceeds even that of overmoded BAW resonators, setting a new high-water mark for frequency-Q product of any room temperature acoustic resonator. The ability to achieve a Q this high at 3-GHz without overmoding, i.e., without the complexity and loss associated with removing unwanted modes, is a significant step forward towards channel-select applications.

References

[1] C. T.-C. Nguyen, "Frequency-selective MEMS for miniaturized low-power communication devices (invited)," *IEEE Trans. Microw. Theory Techn.*, vol. 47, no. 8, pp. 1486–1503, Aug. 1999.

[2] C. T.-C. Nguyen, "MEMS technology for timing and frequency control," *IEEE Trans. Ultrason., Ferroelectr., Freq. Control*, vol. 54, no. 2, pp. 251–270, Feb. 2007.

[3] W. H. W. Tuttlebee, Ed., *Software Defined Radio: Origins, Drivers and International Perspectives*. Hoboken, NJ, USA: Wiley, 2002.

[4] C. T.-C. Nguyen, "MEMS-based RF channel selection for true software-defined cognitive radio and low-power sensor communications," *IEEE Commun. Mag.*, vol. 51, no. 4, pp. 110–119, Apr. 2013.

[5] A. I. Zverev, *Handbook of Filter Synthesis*. Hoboken, NJ, USA: Wiley, 1967.

[6] K. Wang and C. T.-C. Nguyen, "High-order medium frequency micromechanical electronic filters," *J. Microelectromech. Syst.*, vol. 8, no. 4, pp. 534–556, Dec. 1999.

[7] M. Akgul and C. T.-C. Nguyen, "A passband-corrected high rejection channel-select micromechanical disk filter," in *Proc. IEEE Int. Freq. Control Symp. (FCS)*, May 2014, pp. 1–6.

[8] T. J. Cheng and S. A. Bhave, "High-Q, low impedance polysilicon resonators with 10 nm air gaps," in *Proc. IEEE 23rd Int. Conf. Micro Electro Mech. Syst.*, Jan. 2010, pp. 695–698.

[9] F. Ayazi, S. Pourkamali, G. K. Ho, and R. Abdolvand, "High-aspect-ratio SOI vibrating micromechanical resonators and filters," in *IEEE MTT-S Int. Microw. Symp. Dig.*, Jun. 2006, pp. 676–679.

[10] D. Weinstein and S. A. Bhave, "Internal dielectric transduction in bulk-mode resonators," *J. Microelectromech. Syst.*, vol. 18, no. 6, pp. 1401–1408, Dec. 2009.

[11] G. Piazza, P. J. Stephanou, and A. P. Pisano, "Piezoelectric aluminum nitride vibrating contour-mode MEMS resonators," *J. Microelectromech. Syst.*, vol. 15, no. 6, pp. 1406–1418, Dec. 2006.

[12] J. Wang, Z. Ren, and C. T.-C. Nguyen, "1.156-GHz self-aligned vibrating micromechanical disk resonator," *IEEE Trans. Ultrason., Ferroelectr., Freq. Control*, vol. 51, no. 12, pp. 1607–1628, Dec. 2004.

[13] Y. Xie, S.-S. Li, Y.-W. Lin, Z. Ren, and C. T.-C. Nguyen, "1.52-GHz micromechanical extensional wine-glass mode ring resonators," *IEEE Trans. Ultrason., Ferroelectr., Freq. Control*, vol. 55, no. 4, pp. 890–907, Apr. 2008.

[14] J. Wang, J. E. Butler, T. Feygelson, and C. T.-C. Nguyen, "1.51-GHz nanocrystalline diamond micromechanical disk resonator with material-mismatched isolating support," in *Proc. 17th IEEE Int. Conf. Micro Electro Mech. Syst.*, Maastricht, The Netherlands, Jan. 2004, pp. 821–824.

[15] S.-S. Li, Y.-W. Lin, Y. Xie, Z. Ren, and C. T.-C. Nguyen, "Micromechanical 'hollow-disk' ring resonators," in *Proc. 17th IEEE Int. Conf. Micro Electro Mech. Syst.*, Maastricht, The Netherlands, Jan. 2004, pp. 821–824.

[16] T. L. Naing *et al.*, "2.97-GHz CVD diamond ring resonator with $Q > 40,000$," in *Proc. IEEE Int. Freq. Control Symp.*, Baltimore, MD, USA, May 2012, pp. 1–6.

[17] B. Bircumshaw *et al.*, "The radial bulk annular resonator: Towards a 50 Ω RF MEMS filter," in *12th Int. Conf. Solid-State Sens., Actuators Microsyst. Dig. Tech. Papers (TRANSDUCERS)*, Boston, MA, USA, Jun. 2003, pp. 875–878.

[18] F. D. Bannon, III, J. R. Clark, and C. T.-C. Nguyen, "High-Q HF microelectromechanical filters," *IEEE J. Solid-State Circuits*, vol. 35, no. 4, pp. 512–526, Apr. 2000.

[19] S.-S. Li, Y.-W. Lin, Z. Ren, and C. T.-C. Nguyen, "Self-switching vibrating micromechanical filter bank," in *Proc. Joint IEEE Int. Freq. Control/Precision Time Time Interval Symp.*, Vancouver, BC, Canada, Aug. 2005, pp. 135–141.

[20] A. Iula, N. Lamberti, and M. Pappalardo, "A model for the theoretical characterization of thin piezoceramic rings," *IEEE Trans. Ultrason., Ferroelectr., Freq. Control*, vol. 43, no. 3, pp. 370–375, May 1996.

[21] R. Tabrizian, M. Rais-Zadeh, and F. Ayazi, "Effect of phonon interactions on limiting the f.Q product of micromechanical resonators," in *15th Int. Conf. Solid-State Sens. Actuators Dig. Tech. Papers (TRANSDUCERS)*, Denver, CO, USA, Jun. 2009, pp. 2131–2134.

[22] V. B. Braginsky, V. P. Mitrofanov, and V. I. Panov, *Systems With Small Dissipation*. Chicago, IL, USA: Univ. Chicago Press, 1986.

[23] M. Akgul, R. Schneider, Z. Ren, G. Chandler, V. Yeh, and C. T.-C. Nguyen, "Hot filament CVD conductive microcrystalline diamond for high Q, high acoustic velocity micromechanical resonators," in *Proc. Joint Conf. IEEE Int. Freq. Control Eur. Freq. Time Forum*, San Francisco, CA, USA, May 2011, pp. 1–6.

[24] K. Wang, A.-C. Wong, and C. T.-C. Nguyen, "VHF free-free beam high-Q micromechanical resonators," *J. Microelectromech. Syst.*, vol. 9, no. 3, pp. 347–360, Sep. 2000.

[25] Y.-W. Lin, S. Lee, S.-S. Li, Y. Xie, Z. Ren, and C. T.-C. Nguyen, "Series-resonant VHF micromechanical resonator reference oscillators," *IEEE J. Solid-State Circuits*, vol. 39, no. 12, pp. 2477–2491, Dec. 2004.

[26] V. Tas, S. Olcum, M. D. Aksoy, and A. Atalar, "Reducing anchor loss in micromechanical extensional mode resonators," *IEEE Trans. Ultrason., Ferroelectr., Freq. Control*, vol. 57, no. 2, pp. 448–454, Feb. 2010.

[27] M. U. Demirci and C. T.-C. Nguyen, "Higher-mode free-free beam micromechanical resonators," in *Proc. IEEE Int. Freq. Control Symp.*, Tampa, FL, USA, May 2003, pp. 810–818.

[28] R. A. Johnson, *Mechanical Filters in Electronics*. Hoboken, NJ, USA: Wiley, 1983.

[29] L. W. Nagel and D. O. Pederson, "SPICE (simulation program with integrated circuit emphasis)," Dept. EECS, Univ. California, Berkeley, Berkeley, CA, USA, Tech. Rep. ERL-M382, Apr. 1973.

[30] A.-C. Wong and C. T.-C. Nguyen, "Micromechanical mixer-filters ('mixlers')," *J. Microelectromech. Syst.*, vol. 13, no. 1, pp. 100–112, Feb. 2004.

[31] H. C. Nathanson, W. E. Newell, R. A. Wickstrom, and J. R. Davis, Jr., "The resonant gate transistor," *IEEE Trans. Electron Devices*, vol. 14, no. 3, pp. 117–133, Mar. 1967.

[32] M. Akgul, L. Wu, Z. Ren, and C. T.-C. Nguyen, "A negative-capacitance equivalent circuit model for parallel-plate capacitive-gap-transduced micromechanical resonators," *IEEE Trans. Ultrason., Ferroelectr., Freq. Control*, vol. 61, no. 5, pp. 849–869, May 2014.

[33] S. Lee and C. T.-C. Nguyen, "Phase noise amplitude dependence in self-limiting wine-glass disk oscillators," in *Solid-State Sens., Actuator, Microsyst. Workshop Tech. Dig.*, Hiltion Head, SC, USA, Jun. 2004, pp. 33–36.

[34] W. C. Tang, T.-C. H. Nguyen, and R. T. Howe, "Laterally driven polysilicon resonant microstructures," *Sens. Actuators*, vol. 20, pp. 25–32, 1989.

[35] Y.-W. Lin, S.-S. Li, Z. Ren, and C. T.-C. Nguyen, "Low phase noise array-composite micromechanical wine-glass disk oscillator," in *IEEE Int. Electron Devices Meeting Tech. Dig.*, Washington, DC, USA, Dec. 2005, pp. 287–290.

[36] L.-W. Hung and C. T.-C. Nguyen, "Capacitive-Piezoelectric transducers for high-Q micromechanical AlN resonators," *J. Microelectromech. Syst.*, vol. 24, no. 2, pp. 458–473, Apr. 2015.

[37] R. Ruby, "Positioning FBAR technology in the frequency and timing domain," in *Proc. Joint Conf. IEEE Int. Freq. Control Eur. Freq. Time Forum*, San Francisco, CA, USA, May 2011, pp. 1–10.

[38] M. Rinaldi, C. Zuniga, C. Zuo, and G. Piazza, "GHz range nanoscaled AlN contour-mode resonant sensors (CMR-S) with self-sustained CMOS oscillator," in *Proc. Solid-State Sens., Actuators Microsyst. Workshop*, Hilton Head, SC, USA, 2010, pp. 471–474.

[39] R. A. Schneider and C. T.-C. Nguyen, "ON/OFF switchable high-Q capacitive-piezoelectric AlN resonators," in *IEEE Microelectromech. Syst. Conf. Tech. Dig.*, San Francisco, CA, USA, Jan. 2014, pp. 1265–1268.

[40] M. Akgul, B. Kim, Z. Ren, and C. T.-C. Nguyen, "Capacitively transduced micromechanical resonators with simultaneous low motional resistance and $Q > 70,000$," in *Solid-State Sens., Actuator, Microsyst. Workshop Tech. Dig.*, Hilton Head, SC, USA, Jun. 2010, pp. 467–470.

[41] D. T. Nguyen *et al.*, "Improved optomechanical disk resonator sitting on a pedestal mechanical shield," *New J. Phys.*, vol. 17, no. 2, p. 023016, 2015.

[42] S. Galliou, M. Goryachev, R. Bourquin, P. Abbé, J. P. Aubry, and M. E. Tobara, "Extremely low loss phonon-trapping cryogenic acoustic cavities for future physical experiments," *Sci. Rep.*, vol. 3, Mar. 2013, Art. ID 2132.

[43] G. R. Kline, K. M. Lakin, and K. T. McCarron, "Overmoded high Q resonators for microwave oscillators," in *Proc. IEEE Int. Freq. Control Symp.*, Jun. 1993, pp. 718–721.

[44] T.-T. Yen, A. P. Pisano, and C. T.-C. Nguyen, "High-Q capacitive-piezoelectric AlN Lamb wave resonators," in *Proc. IEEE 26th Int. Conf. Micro Electro Mech. Syst. (MEMS)*, Jan. 2013, pp. 114–117.

[45] E. Hwang and S. A. Bhave, "Transduction of high-frequency micromechanical resonators using depletion forces in p-n diodes," *IEEE Trans. Electron Devices*, vol. 58, no. 8, pp. 2770–2776, Aug. 2011.

[46] T. O. Rocheleau, T. L. Naing, Z. Ren, and C. T.-C. Nguyen, "Acoustic whispering gallery mode resonator with $Q > 109,000$ at 515 MHz," in *Proc. 25th IEEE Int. Conf. Micro Electro Mech. Syst.*, Paris, France, Jan./Feb. 2012, pp. 672–675.

[47] C.-M. Lin, Y.-Y. Chen, V. V. Felmetsger, D. G. Senesky, and A. P. Pisano, "AlN/3C–SiC composite plate enabling high-frequency and high-Q micromechanical resonators," *Adv. Mater.*, vol. 24, no. 20, pp. 2722–2727, May 2012.

Thura Lin Naing received the B.S. and Ph.D. degrees in electrical engineering and computer sciences from the University of California at Berkeley, in 2007 and 2015, respectively. His Ph.D. work was on low-power signal processors using capacitive-gap MEMS resonator-based oscillator systems. During his Ph.D., he contributed to dozens of publications and received the Best Student Paper Award at the 2013 Joint UFFC, EFTE, and PFM Symposium for his work on a GSM phase noise-compliant low power oscillator. His research interests focus on mixed-signal integrated circuits, microelectromechanical systems (MEMS), system integration of MEMS and IC circuits, low-power signal processors, and MEMS-based oscillators. He is currently pursuing commercialization of low power radios based on his Ph.D. research.

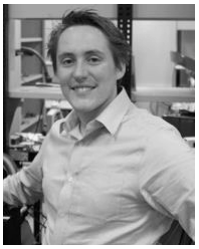

Tristan O. Rocheleau received the B.S. (Hons.) degree in physics from the University of California, Santa Barbara, in 2005, and the Ph.D. degree in physics from Cornell University with a focus on cooling mesoscopic mechanical resonators toward their quantum ground state in 2011. Subsequently, he joined the Clark T.-C. Nguyen's Group, Electrical Engineering and Computer Science Department, University of California at Berkeley, as a Postdoctoral Fellow, working on projects related to radio-frequency microelectromechanical systems (MEMS). His research interests include integrated micromechanical and CMOS systems, optomechanical oscillator, and signal converts and MEMS applications in low power radio receiver components. He contributed to dozens of publications and received the best paper award at the MEMS 2013 conference for his work on improved optomechanical oscillators.

Zeying Ren (M'04) received the B.S. and M.S. degrees in electrical engineering from Tianjin University, Tianjin, China, in 1987 and 1990, respectively.

From 1990 to 1998, she was a Process Engineer with the National Research Center for Optoelectronics (NCOT), Institute of Semiconductors, Chinese Academy of Science, Beijing, China. She was a Research Scholar in the Department of Electrical and Computer Engineering, Northwestern University, Evanston, IL, USA, from 1998 to 2000. From 2001 to 2002, she was with Nanovation Technologies, as a Process Engineer. From 2002 to 2007, she was with the Solid-State Electronics Laboratory as an Engineer in Research in the Department of Electrical Engineering and Computer Science, University of Michigan, Ann Arbor. In 2008, she joined Prof. Clark Nguyen's research group as a Process Engineer at the University of California, Berkeley, where she conducted MEMS fabrication at the Marvell Nanofabrication Laboratory until 2014. She is now a Process Engineer with Crossbar, Inc., Santa Clara, CA.

Sheng-Shian Li (S'04–M'07) received the B.S. and M.S. degrees in mechanical engineering from National Taiwan University, in 1996 and 1998, respectively, and the M.S. and Ph.D. degrees in electrical engineering and computer science from the University of Michigan, Ann Arbor, MI, USA, in 2004 and 2007, respectively. In 2007, he joined RF Micro Devices, Greensboro, NC, USA, where he was a Research and Development Senior Design Engineer until mid-2008 for the development of MEMS resonators and filters. In 2008, he joined the Institute of NanoEngineering and MicroSystems, National Tsing Hua University, Hsinchu, Taiwan, where he is currently a Professor. His research interests focus on nano/microelectromechanical systems, integrated resonators and sensors, RF MEMS, CMOS-MEMS technology, front-end communication architectures, and integrated circuit design and technology.

Dr. Li received the Teaching Excellence Award from the College of Engineering, National Tsing Hua University, in 2011. In 2013, he received the Young Faculty Research Award from National Tsing Hua University, and the Ta-Yu Wu Memorial Award from the Ministry of Science and Technology of Taiwan. Together with his students, he received the Best Student Paper Awards at the 2011 IEEE International Frequency Control Symposium and the 2012 IEEE Sensors Conference. He served on the TPC of the IEEE International Frequency Control Symposium (IFCS), the IEEE Sensors Conference, and the Transducers Conference. He also served as the Local Organizing Committee Chair at the 2014 IFCS and the TPC Vice Chair (Group 1) in the 2016 IFCS, respectively.

Clark T.-C. Nguyen (S'90–M'95–SM'01–F'07) received the B.S., M. S., and Ph.D. degrees from the University of California at Berkeley, in 1989, 1991, and 1994, respectively, all in electrical engineering and computer sciences.

He joined as a Faculty Member with the University of Michigan, Ann Arbor, in 1995, where he was a Professor with the Department of Electrical Engineering and Computer Science until 2006. In 2006, he joined the Department of Electrical Engineering and Computer Sciences, University of California at Berkeley, where he is currently a Professor and the Co-Director of the Berkeley Sensor and Actuator Center. His research interests focus on microelectromechanical systems (MEMS), and include integrated micromechanical signal processors and sensors, merged circuit/micromechanical technologies, optomechanical devices, RF communication architectures, and integrated circuit design and technology. In 2001, he founded Discera, Inc., a company aimed at commercializing communication products based upon MEMS technology, with an initial focus on the very vibrating micromechanical resonators pioneered by his research in past years. He served as the Vice President and Chief Technology Officer of Discera until 2002, at which point he joined the Defense Advanced Research Projects Agency (DARPA) on an IPA, where he served for almost four years as the Program Manager of the MEMS, micro power generation, chip-scale atomic clock, MEMS exchange, harsh environment robust micromechanical technology, micro gas analyzers, radio isotope micropower sources, RF MEMS improvement, navigation-grade integrated micro gyroscopes, and micro cryogenic coolers programs, with the Microsystems Technology Office.

Prof. Nguyen received the Cady Award in 2006, and together with his students, has garnered more than ten best paper awards from IEEE conferences and journals focused on frequency control and MEMS. From 2007 to 2009, he served as a Distinguished Lecturer of the IEEE Solid-State Circuits Society. He was the Technical Program Chair of the 2010 IEEE International Frequency Control Symposium and a Co-General Chair of the 2011 Combined IEEE International Frequency Control Symposium, and European Frequency and Time Forum. From 2008 to 2013, he served as the Vice President of Frequency Control in the IEEE Ultrasonics, Ferroelectrics, and Frequency Control Society, and is currently the President-Elect of the IEEE Ultrasonics, Ferroelectrics, and Frequency Control Society.